



NAVAL
POSTGRADUATE
SCHOOL

MONTEREY, CALIFORNIA

THESIS

MICROWAVE ESTIMATES OF THE EXTRATROPICAL TRANSITIONS
PROCESS

by

Cedrick L. Stubblefield

March 2005

Thesis Advisor:
Second Reader:

Patrick Harr
Phil Durkee

Approved for public release; distribution is unlimited

THIS PAGE INTENTIONALLY LEFT BLANK

REPORT DOCUMENTATION PAGE		Form Approved OMB No. 0704-0188	
Public reporting burden for this collection of information is estimated to average 1 hour per response, including the time for reviewing instruction, searching existing data sources, gathering and maintaining the data needed, and completing and reviewing the collection of information. Send comments regarding this burden estimate or any other aspect of this collection of information, including suggestions for reducing this burden, to Washington headquarters Services, Directorate for Information Operations and Reports, 1215 Jefferson Davis Highway, Suite 1204, Arlington, VA 22202-4302, and to the Office of Management and Budget, Paperwork Reduction Project (0704-0188) Washington DC 20503.			
1. AGENCY USE ONLY (Leave blank)	2. REPORT DATE March 2005	3. REPORT TYPE AND DATES COVERED Master's Thesis	
4. TITLE AND SUBTITLE: Microwave Estimates of the Extratropical Transition Process		5. FUNDING NUMBERS	
6. AUTHOR(S) Cedrick L. Stubblefield			
7. PERFORMING ORGANIZATION NAME(S) AND ADDRESS(ES) Naval Postgraduate School Monterey, CA 93943-5000		8. PERFORMING ORGANIZATION REPORT NUMBER	
9. SPONSORING /MONITORING AGENCY NAME(S) AND ADDRESS(ES) N/A		10. SPONSORING/MONITORING AGENCY REPORT NUMBER	
11. SUPPLEMENTARY NOTES The views expressed in this thesis are those of the author and do not reflect the official policy or position of the Department of Defense or the U.S. Government.			
12a. DISTRIBUTION / AVAILABILITY STATEMENT Approved for public release; distribution is unlimited		12b. DISTRIBUTION CODE	
13. ABSTRACT (maximum 200 words) Microwave satellite imagery is a valuable tool for the observation of mature tropical cyclones. This study examined the application of microwave data to the extratropical transition (ET) process. During ET a tropical cyclone (TC) moves into an area of large gradients in many atmospheric parameters. The data sparse regions in which these gradients exist make the examination of key physical mechanisms responsible for the ET process difficult. The Advanced Microwave Sounding Unit (AMSU) was used to investigate temperature and water vapor gradients. Advanced Microwave Scanning Radiometer was used to examine WV gradients and precipitation intensities. These observations were combined with diagnostic analysis of frontogenesis during the ET process of a TC that re-intensified as an extratropical cyclone and a TC that dissipated. Although the different outcomes of ET were related to differences in coupling between the decaying TC and the midlatitude environment, microwave data were useful for defining specific characteristics that either inhibited or enhanced the coupling of the decaying TC with the midlatitude environment.			
14. SUBJECT TERMS Tropical cyclones, Extratropical Transition, Advanced Microwave Sounding Unit, Advanced Microwave Scanning Radiometer, Polar-orbiting satellites, Frontogenesis		15. NUMBER OF PAGES 87	16. PRICE CODE
17. SECURITY CLASSIFICATION OF REPORT Unclassified		18. SECURITY CLASSIFICATION OF THIS PAGE Unclassified	
19. SECURITY CLASSIFICATION OF ABSTRACT Unclassified		20. LIMITATION OF ABSTRACT UL	

THIS PAGE INTENTIONALLY LEFT BLANK

Approved for public release; distribution is unlimited

MICROWAVE ESTIMATES OF THE EXTRATROPICAL TRANSITIONS
PROCESS

Cedrick L. Stubblefield
Captain, United States Air Force
B.S., Florida State University, 1999

Submitted in partial fulfillment of the
requirements for the degree of

MASTER OF SCIENCE IN METEOROLOGY

from the

NAVAL POSTGRADUATE SCHOOL
March 2005

Author: Cedrick L. Stubblefield

Approved by: Patrick Harr
Thesis Advisor

Phil Durkee
Co-Advisor

Phil Durkee
Chairman, Department of Meteorology

THIS PAGE INTENTIONALLY LEFT BLANK

ABSTRACT

Microwave satellite imagery is a valuable tool for the observation of mature tropical cyclones. This study examined the application of microwave data to the extratropical transition (ET) process. During ET a tropical cyclone (TC) moves into an area of large gradients in many atmospheric parameters. The data sparse regions in which these gradients exist make the examination of key physical mechanisms responsible for the ET process difficult. The Advanced Microwave Sounding Unit (AMSU) was used to investigate temperature and water vapor gradients. Advanced Microwave Scanning Radiometer was used to examine WV gradients and precipitation intensities. These observations were combined with diagnostic analysis of frontogenesis during the ET process of a TC that re-intensified as an extratropical cyclone and a TC that dissipated. Although the different outcomes of ET were related to differences in coupling between the decaying TC and the midlatitude environment, microwave data were useful for defining specific characteristics that either inhibited or enhanced the coupling of the decaying TC with the midlatitude environment.

THIS PAGE INTENTIONALLY LEFT BLANK

TABLE OF CONTENTS

I.	INTRODUCTION	1
A.	MOTIVATION	2
B.	DEFINITIONS	4
C.	CLIMATOLOGY	6
D.	GOALS	7
II.	INSTRUMENTS	9
A.	ADVANCED MICROWAVE SOUNDING UNIT	9
1.	AMSU-A	10
2.	AMSU-B	11
B.	ADVANCED MICROWAVE SCANNING RADIOMETER FOR (EOS) ..	16
III.	DATA	17
A.	INTENSITY ESTIMATING TOOLS	17
1.	Limitations of Numerical Forecast Models	17
2.	Limitations of IR and Visible Imagery	18
3.	Limitations of Microwave Imagery	19
B.	DATA PROCESSING	20
1.	AMSU-A Temperature Measurement	21
2.	AMSU-A Antenna Correction	22
3.	AMSU-A Limb Correction	23
IV.	RESULTS	25
A.	TOKAGE	27
1.	Synoptic Overview	27
2.	Diagnostics	35
B.	MA-ON	48
1.	Synoptic Overview	48
2.	Diagnostics	56
V.	CONCLUSION	63
	LIST OF REFERENCES	67
	INITIAL DISTRIBUTION LIST	71

THIS PAGE INTENTIONALLY LEFT BLANK

LIST OF FIGURES

Figure 1.	Schematic view of some of the terminology used to describe the extratropical transition process. According to this view, all poleward-moving TCs experience a transformation. This either leads to decay or to some type of transition (e.g., simple, complex, compound) to an extratropical cyclone.	5
Figure 2.	The AMSU-A channel frequency bands (vertical lines) as compared to the standard atmospheric water vapor and oxygen windows (curved solid lines).	11
Figure 3.	AMSU-A weighting function diagram	14
Figure 4.	Schematic of AMSU-B channel frequency bands (vertical lines) as compared to the standard atmospheric water vapor and oxygen windows (curved solid lines).	15
Figure 5.	(a) IR and (b) WV imagery at 0000 UTC 20 Oct 2004; (c) 500 hPa height (m) and MSLP (hPa); (d) 200 hPa wind (m s^{-1}) and MSLP (hPa); and (e) 500 hPa potential temperature (K) and omega ($\mu\text{b s}^{-1}$) All gridded fields are from the NOGAPS analysis at 0000 UTC 20 Oct 2004.	29
Figure 6.	As in Figure 5, except for 1200 UTC 20 Oct 2004.	30
Figure 7.	As in Figure 5, except for 0000 UTC 21 Oct 2004.	32
Figure 8.	As in Figure 5, except for 1200 UTC 21 Oct 2004.	34
Figure 9.	(a) NOGAPS 6-h forecast of 500 hPa height (m) valid at 1800 UTC 20 Oct and a channel 7 brightness temperature composite of two separate AMSU-A passes between 1600 and 1800 UTC 20 Oct (shaded) (b) enhanced IR at 1800 UTC 20 Oct.	36
Figure 10.	Analyzed potential temperature (K) and F_s vectors (left column) and F_n vectors (right column) at 850 hPa (top row), 700 hPa (middle row), and 500 hPa (bottom row) for 1800 UTC 20 Oct 2004. Vector magnitudes are defined by the scale vector in the lower right of each panel. Units are $\text{K m}^{-1} \text{s}^{-1}$. Contours define the divergence of F_n and F_s vectors and are units of $\mu\text{b s}^{-1}$. Shaded regions are AMSR-E derived rain rate (in mm h^{-1})	38
Figure 11.	The AMSR-E derived WV at 1800 UTC 20 Oct 2004 and NOGAPS analysis of potential temperature (contour interval 2 K), F_n ($\text{K m}^{-1} \text{s}^{-1}$)	40

Figure 12.	As in Figure 10, except for 0000 UTC 21 Oct 2004.	41
Figure 13.	Channel 7 AMSU-A brightness temperature (shaded) with 500 hPa height(contour 60 m) at 0600 UTC 21 Oct 2004.	42
Figure 14.	As in Figure 10, except for 1200 UTC 21 Oct 2004.	45
Figure 15.	As in Figure 13, except for 1800 UTC 21 Oct 2004.	46
Figure 16.	As in Figure 5, except for Typhoon Ma-on on 0000 UTC 9 Oct 2004.	49
Figure 17.	As in Figure 5, except for 1200 UTC 9 Oct 2004. ..	51
Figure 18.	As in Figure 5, except for 0000 UTC 10 Oct 2004.	53
Figure 19.	As in Figure 5, except for 1200 UTC 10 Oct 2004.	54
Figure 20.	(a) NOGAPS 6-h forecast of 500 hPa height (m) valid at 0600 UTC 20 Oct and a channel 7 brightness temperature composite of two separate AMSU-A passes between 1600 and 1800 UTC 20 Oct (shaded) (b) enhanced IR at 0600 UTC 20 Oct.	56
Figure 21.	As in Figure 10, except for Typhoon Ma-on 0000 UTC 9 Oct 2004.	57
Figure 22.	As in Figure 11, except for 0000 UTC 09 Oct 2004.	58
Figure 23.	As in Figure 10, except for 0000 UTC 10 Oct 2004.	61

LIST OF TABLES

Table 1.	Tropical Cyclone Basins(Foley, 1989).	1
Table 2.	Climatology of TC movement into the midlatitudes by basin, compiled from recent season summaries (Foley, 1989).	6
Table 3.	AMSU-A Channel Characteristics (Goodrum 2004)	13
Table 4.	AMSU-B Channel Characteristics (Goodrum 2004)	15
Table 5.	AMSR-E Channel Characteristics (From http://www.ghcc.msfc.nasa.gov/AMSR/)	16

THIS PAGE INTENTIONALLY LEFT BLANK

ACKNOWLEDGMENTS

Many people have contributed to the successful completion of my graduate education. I would like to thank my teachers, family, colleagues, and friends who have been instrumental in my scholastic development.

The information obtained from the instructors at the Naval Postgraduate School has empowered me. The entire department displayed competence, a high degree of technical expertise, and professionalism at all times. I now have a greater understanding and more confidence in my knowledge of the theories and applied principles of atmospheric sciences.

Professor Patrick Harr, my thesis advisor, was invaluable to my success. His patience, genuine concern, and self-sacrifice have not gone unnoticed.

To my colleagues and friends, your enthusiasm was an inspiration to me and facilitated the learning process. Thanks.

To my extended family, your support fueled my drive for excellence. Tamico, Cedrick Jr., and Kyle, your flexibility and understanding were not only important but the key to my success. We did it!

THIS PAGE INTENTIONALLY LEFT BLANK

I. INTRODUCTION

Every year tropical cyclones (TCs) develop in low latitude regions of one of seven "basins" around the globe (Table 1). Many TCs move to higher latitudes during their life cycle. This poleward track takes the TC away from its heat source into a region of colder sea surface temperatures and larger vertical wind shear. In certain basins, as in the Atlantic and Northwest Pacific basins, the northwestward track often takes the TC over land. After encountering cooler sea surface temperatures and/or strong vertical wind shear or moving onshore, TCs may undergo a period of weakening and subsequently dissipate. This is the case with over three-fourths of TCs crossing 30 deg lat (Evans and Hart 2003). The remaining one-fourth of TCs passing into the middle latitudes interact directly with the baroclinic environment of the midlatitudes and take on extratropical characteristics (Brand and Guard 1978; Muramatsu 1985).

Table 1. Tropical Cyclone Basins (Foley, 1989).	
1.	Atlantic basin (including the North Atlantic Ocean, the Gulf of Mexico, and the Caribbean Sea)
2.	Northeast Pacific basin (from Mexico to about the dateline)
3.	Northwest Pacific basin (from the dateline to Asia including the South China Sea)
4.	North Indian basin (including the Bay of Bengal and the Arabian Sea)
5.	Southwest Indian basin (from Africa to about 100E)
6.	Southeast Indian/Australian basin (100E to 142E)
7.	Australian/Southwest Pacific basin (142E to about 120W)

Muramatsu (1985) noted that movement of a TC into the midlatitudes results in several characteristic structure changes. These were identified as

1. temperature and moisture fields developed distinct asymmetries
2. the organized core convection becomes disrupted and disappears
3. the circulation in middle and upper levels becomes disrupted and weakens
4. the major precipitation bands shift towards the front eastward quadrant of the storm
5. ahead of the TC, dry, cold air intrudes into the circulation
6. the area of gale-force winds expands and becomes highly asymmetric

A. MOTIVATION

The extratropical transition (ET) of a TC affects its track, speed, intensity, size, and landfall probability. Cyclones that undergo ET often become fast-moving and rapidly-developing extratropical cyclones (Jones et al. 2003). The potential for these factors to produce gale-force winds and extremely heavy precipitation in the midlatitudes makes these events acutely important to insurers, civilian governments, coastal populations, and the warfighter.

The results of a TC making landfall during the ET process have been well documented. Natural disasters such as the ETs of Hurricane Floyd in 1999 (Atallah and Bosart 2003), Tropical Storm Agnes in 1972 (DiMego and Bosart 1982a,b), Hurricane Hazel in 1954 (Palmen 1958), and the

"1938" Hurricane (Pierce 1939) were associated with interactions of decaying TCs with a baroclinic environment in the midlatitudes that resulted in extreme precipitation totals of 200-300 mm over a period as short as 18 h (Jones et al. 2003). President Bush, in response to the landfalls of hurricanes Charley, Frances, Ivan and Jeanne along the Florida coasts in 2004, made a \$12.2 billion hurricane relief request that included \$889 million for storm-related expenses at military bases. These storms occurred over a period of about 43 days, but a single ET event is quite capable of causing mass flooding, billions of dollars in damages, and loss of life. Therefore, accurate forecasts of intensity and movement of TCs undergoing ET are critical.

Accurate TC forecasts are highly dependent on the accuracy of the current TC intensity and position. The challenge is observing the atmospheric parameters and large gradients associated with TCs. The various ocean basins where TCs develop and/or decay are data sparse regions, which limit the efficiency of TC initialization. However, the introduction of remotely-sensed data has improved observation capabilities over these ocean basins. Infrared (IR) and visible imagery can provide some clues to the atmospheric dynamics associated with of a TC. Water-vapor (WV) imagery can be used to identify outflow into the midlatitudes. However, these techniques are not useful in resolving multi-level environmental gradients. This is the strength of microwave imagery. Unlike IR and WV imagery, microwave imagery from polar-orbiting satellites can be used to examine the parameters and gradients of a TC and its environment unobstructed by distributions of cloud.

B. DEFINITIONS

There is no commonly accepted definition of ET, but there have been attempts to characterize storm development and maturation. Matano and Sekioka (1971) characterized two types of ET in the western North Pacific based on surface pressure analyses. The first characterization is called a "complex transition". This transition occurs when a TC interacts with a pre-existing midlatitude front or trough. The second is a "compound" transition, which results when a TC interacts or appears to merge with a midlatitude cyclone. A third, identified by Brand and Guard (1979), occurs when the TC dissipates while moving into the midlatitude environment.

Klein et al. (2000) studied cases of ET during July-October 1994-96 in the western North Pacific and determined that an ET has two stages. Because the vast majority of the cases they studied appeared to transform from a warm-core vortex into a baroclinic, extratropical cyclone in the same sequential fashion, they identified the first stage as the "transformation" stage. The second stage is identified as the period in which the decaying TC may re-intensify. However, not all decaying TCs will re-intensify as some will dissipate (Figure 1).

Whether the decaying TC re-intensifies or dissipates is a function of several factors. The physical mechanisms found to favor extratropical re-intensification include an upper-level midlatitude trough approaching from the west, the presence of a lower-tropospheric horizontal temperature gradient, and distribution of water vapor. Land-falling TCs often experience increased surface drag, a reduction of surface fluxes of latent and sensible heat, and orographic

perturbations to the flow (Jones et al. 2003). These factors may contribute to subsequent dissipation.

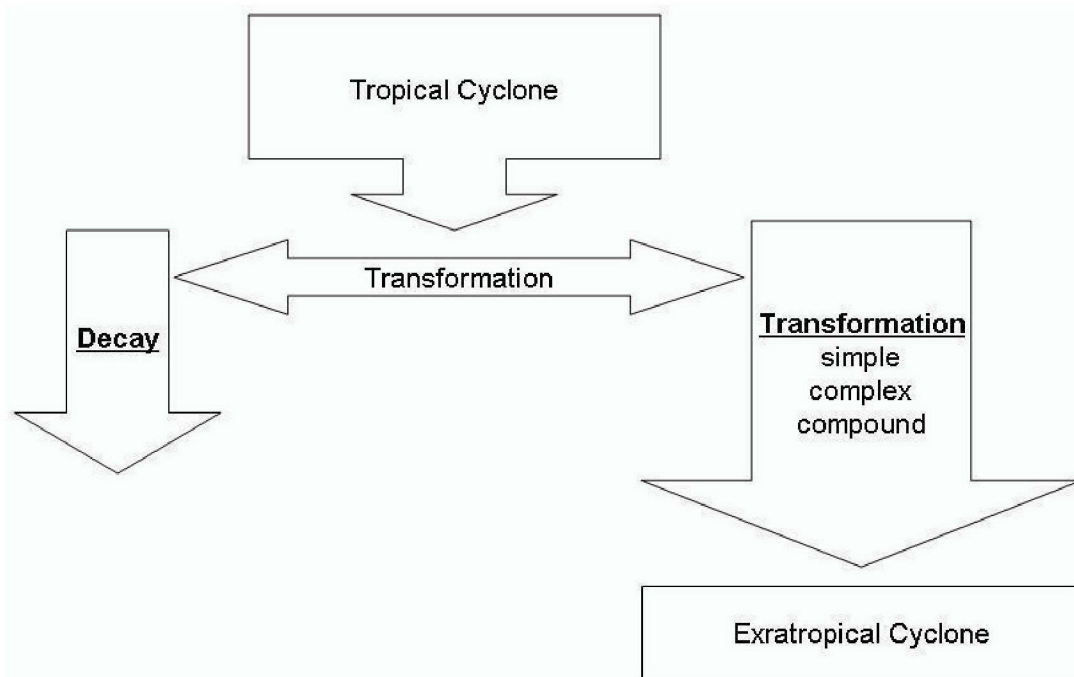


Figure 1. Schematic view of some of the terminology used to describe the extratropical transition process. According to this view, all poleward-moving TCs experience a transformation. This either leads to decay or to some type of transition (e.g., simple, complex, compound) to an extratropical cyclone.

Harr and Elsberry (2000) related two dominant characteristic midlatitude circulation patterns to 30 ET cases studied in the western North Pacific during June-October 1994-97. The first pattern is the northwest pattern. It is defined such that the ET occurs downstream of a midlatitude trough such that the primary midtropospheric potential vorticity maximum is northwest of the decaying TC. In the second case (the northeast pattern), the midlatitude trough west of the decaying TC is weak and the midlatitude circulation is dominated by a large quasi-stationary cyclone northeast of the TC center.

Ultimately, an ET is a gradual process in which a TC loses tropical characteristics and becomes more extratropical in nature. As previously mentioned, this transition is set in motion by environmental changes that occur as the TC moves northward. During ET, the TC often experiences acceleration and/or re-intensification. Understanding and categorizing the weather parameters responsible for the initiation of an ET is a complex processes. However, identification of key parameters is critical to early identification of the cyclones that will most likely experience a transition.

Table 2. Climatology of TC movement into the midlatitudes by basin, compiled from recent season summaries (Foley, 1989).								
				Poleward of				
Region	Years	Cyclones		25	30	35	40	45
NW Pacific	5	132		66	49	27	8	0
NE Pacific	4	74		9	1	0	0	0
Atlantic	4	37		32	31	24	15	9
S. Pacific	4	54		32	19	10	0	0
S. Indian	4	68		17	8	4	1	0
N. Indian	5	26		0	0	0	0	0

C. CLIMATOLOGY

During 1990-1997 over the western North Pacific, at least one ET occurred in all months except February (Harr and Elsberry 2000). On average, ET in the Southern Hemisphere is completed by 30°S (Sinclair 2002), but storms in the Northern Hemisphere may preserve tropical characteristics as far north as 50°N (Jones et al. 2003). Evans and Hart (2003) estimated that 45% of Atlantic tropical storms undergo a transition -- more than any other

basin). Their results showed that over 60% of TCs that undergo ET maintain their intensity or strengthen.

Klein et al. (2000) found that 30 out of 112 TCs in the Northwest Pacific from 1 June through 31 October during 1994-1997 completed ET. It was noted that 25 recurved and subsequently re-intensified. Of those that re-intensified, 6 were typhoons, 5 were supertyphoons, and nineteen were tropical storms. Thirteen of the 30 cases translated into a northeast pattern and 17 translated into a northwest pattern, as defined by Harr et al. (2000), with the northwest cases resulting in a significantly lower sea-level pressure than the northeast cases.

D. GOALS

The primary objective of this study is to explore the benefits of microwave imagery in examining the ET process. As stated above, the re-intensification process depends on various environmental factors. Many of these factors involve gradients of parameters that are not easily observed with current "in situ" observational systems due to the limited availability of observation sites in ocean regions. Therefore, remotely sensed data of important environmental conditions might define important factors that would aid in the prediction of subsequent ET characteristics.

Section II describes several satellite microwave instruments. We examine the scan geometry of these instruments and their respective channel frequencies as they relate to the microwave data used in examination of the ET process. In section III, the focus is on the methods used to process the data for this study. Limitations on numerical model and satellite forecast

estimates are discussed along with the anticipated limitations of microwave estimates of the ET process. Section IV examines two ET cases with respect to diagnostics based on numerical model analysis and the use of microwave data to examine the environment of the ET. Finally, the findings of this study are summarized in section V.

II. INSTRUMENTS

Microwave instruments have been placed on numerous earth- observing satellite platforms in recent years. Because microwaves have very long wavelengths (low frequencies), they pass through clouds relatively easily but are sensitive to precipitation-size drops. Two gases, oxygen and water vapor, absorb microwave photons depending on their frequency. Figure 2 shows the atmospheric transmittance through a gaseous atmosphere for the microwave wavelength/frequency domain. Therefore, microwave imagery provides information on water vapor concentrations and atmospheric temperature (from oxygen emission), both essential in investigating the ET process. The Advanced Microwave Sounding Unit (AMSU) and the Advanced Microwave Scanning Radiometer (AMSR) are among the most recent microwave satellite instruments deployed and were used exclusively in this study.

A. ADVANCED MICROWAVE SOUNDING UNIT

The AMSU instrument was first launched on the National Oceanic and Atmospheric Administration (NOAA) polar orbiting satellite NOAA-15 in May 1998, NOAA-16 in September 2000, and NOAA-17 in June 2002 as part of the NOAA ATVOS (Advanced Television Infrared Observation Satellite (TIROS) Operational Vertical Sounder (TOVS)) system. The instrument was also launched on Aqua, National Aeronautics and Space Administration's (NASA) latest Earth observing satellite (EOS), in May 2002. The AMSU instrument has two sounders. The AMSU temperature (AMSU-A) and moisture (AMSU-B) sounders measure the outgoing radiances from the atmosphere and the earth surface.

Together the AMSU-A and AMSU-B sensors provide 20 channels of microwave radiances. A complete description of AMSU-A and AMSU-B can be found in the NOAA KLM user's guide (Goodrum et al. 2004).

1. AMSU-A

The AMSU-A is a cross-track, line-scanned instrument. The receiving antennas are continuously rotating, parabolic focusing reflectors with a complete rotation time of eight seconds. The instrument scans the Earth from 30 different angles for six seconds and rapidly scans a cold space view and an internal (warm) blackbody calibration target during the remaining two seconds. This gives the instrument an instantaneous field of view (IFOV) of 3.3 degrees (circular), a 1690 km swath (a 2,343 km swath width from the 833 km nominal orbital altitude), and a spatial resolution of 40 km horizontal at nadir.

The AMSU-A is designed to measure the atmospheric temperature profile from 0 to 40 km and provide atmospheric water vapor and precipitation estimates. It is a fifteen-channel radiometer comprised of two separate modules, AMSU-A1 and AMSU-A2. The AMSU-A1 senses data for channels 3-14 between 50.3-57.29 GHz and channel 15 at 89.0 GHz. AMSU-A2 senses data for channels 1 and 2 at 23.8 and 31.4 GHz, respectively (see Figure 2).

As illustrated in Figure 2, channel 1 is in the middle of a water vapor absorption band which makes it ideal for estimating atmospheric water vapor content. Channel 2 is in a relative absorption window and is sensitive to wind speed and precipitation. Channels 3-14 are in a strong oxygen absorption band. The channels closer to the edge of the window (channels 3-4) will retrieve radiance values

from the surface and the lower atmosphere. As the channels move closer to the center of the window (channels 5-14), however, the radiance reaching the sensor originates from higher in the atmosphere as illustrated by the weighting functions of Figure 3. Because the weighting function of channel 7 peaks in the upper troposphere, it was used to study upper-level TC structures. Channel 15, another relative absorption window but at shorter wavelength (higher frequency), is sensitive to cloud properties including precipitation.

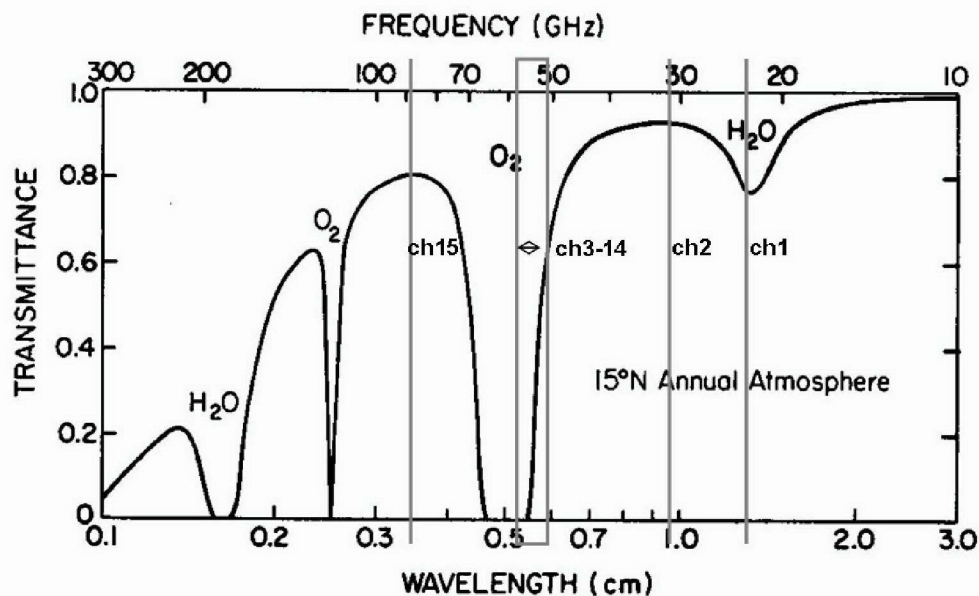


Figure 2. The AMSU-A channel frequency bands (vertical lines) as compared to the standard atmospheric water vapor and oxygen windows (curved solid lines).

2. AMSU-B

The AMSU-B covers channels 16-20 of the AMSU instrument. This five-channel radiometer is designed to measure the humidity from a number of different atmospheric layers (Figure 4). As listed in Table 4, Channels 18, 19, and 20 retrieve radiances in the 183 GHz water vapor absorption band. Channels 16 and 17 are in relative absorption windows and penetrate deeper though the

atmosphere and retrieve radiance from near the Earth's surface.

Table 3. AMSU-A Channel Characteristics (Goodrum 2004)				
Chan. #	Channel Frequency (MHz)	# bands	Polarization at nadir (See Note 1)	Function
AMSU-A1				
1	23,800	1	Vertical	Water Vapor Burden
2	31,400	1	Vertical	Surface Temperature
AMSU-A2				
3	50,300	1	Vertical	Surface Temperature
4	52,800	1	Vertical	Surface Temperature
5	53596±115	2	Horizontal	Tropospheric Temp
6	54,400	1	Horizontal	Tropospheric Temp
7	54,940	1	Vertical	Tropospheric Temp
8	55,500	1	Horizontal	Tropospheric Temp
9	$f_0=57,290.344$	1	Horizontal	Stratospheric Temp
10	$f_0\pm217$	2	Horizontal	Stratospheric Temp
11	$f_0\pm322.2\pm48$	4	Horizontal	Stratospheric Temp
12	$f_0\pm322.2\pm22$	4	Horizontal	Stratospheric Temp
13	$f_0\pm322.2\pm10$	4	Horizontal	Stratospheric Temp
14	$f_0\pm322.2\pm4.5$	4	Horizontal	Stratospheric Temp
15	89,000	1	Vertical	Cloud Top/Snow

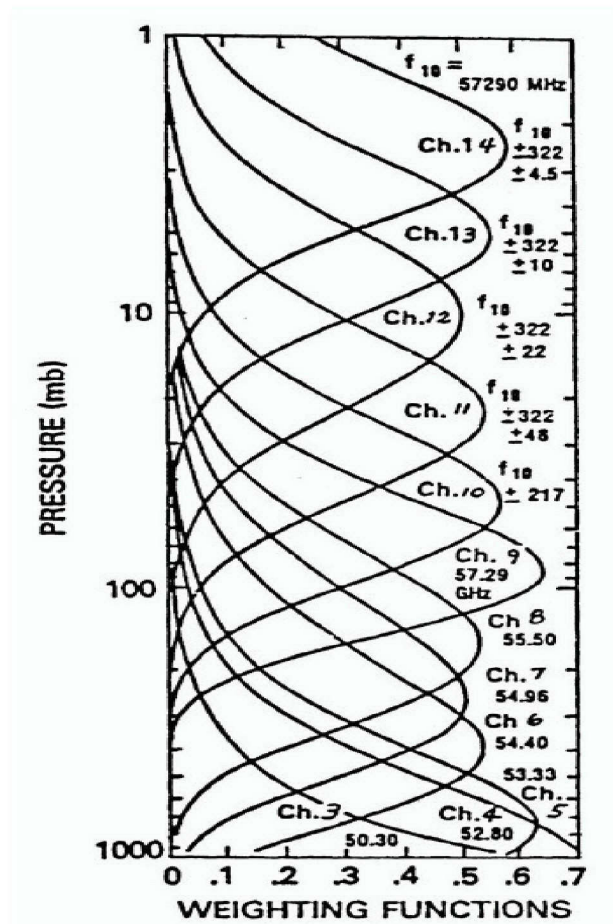


Figure 3. AMSU-A weighting function diagram

The AMSU-B is a cross-track, line-scanned instrument that consists of a parabolic reflector antenna. The antennas are rotated ever 2.67 seconds and the incoming radiation is focused into the receiver assembly. The antenna beams continuously scan in a plane perpendicular to the instrument with a beamwidth of a constant 1.1 degrees. The sampling method of the module translates to a 16 km resolution at nadir at a nominal altitude of 850 km.

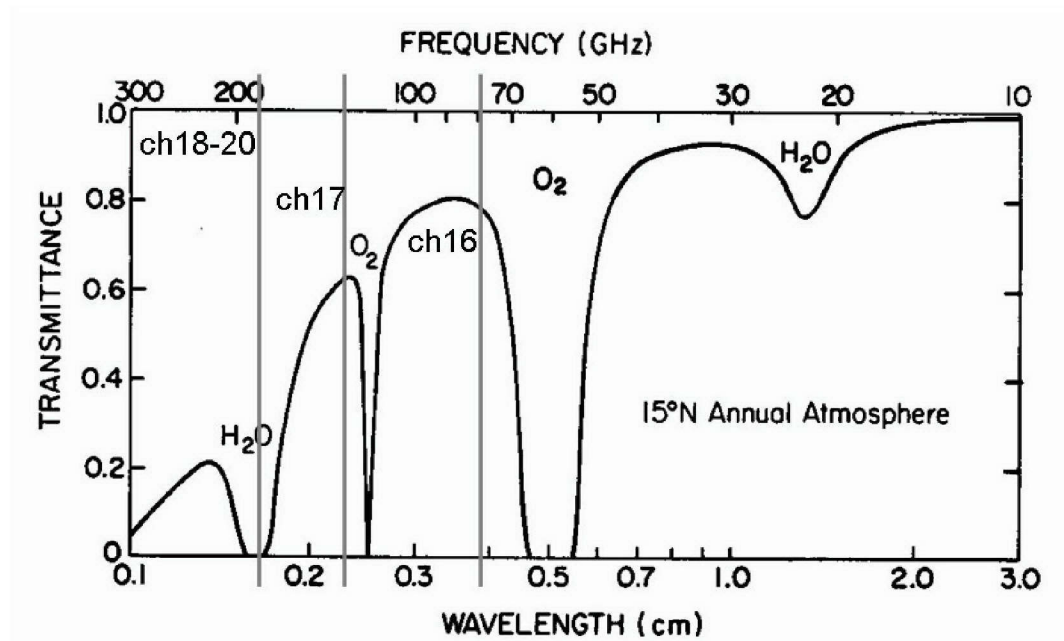


Figure 4. Schematic of AMSU-B channel frequency bands (vertical lines) as compared to the standard atmospheric water vapor and oxygen windows (curved solid lines).

Table 4. AMSU-B Channel Characteristics (Goodrum 2004)				
Channel number	Center freq. of channel (GHz)	No. of pass bands	NEAT (see Note 1) (K)	Polarization angle (see Note 2)
16	89.0±0.9	2	0.37	90-θ
17	150.0±0.9	2	0.84	90-θ
18	183.31±1.00	2	1.06	90-θ
19	183.31±3.00	2	0.70	90-θ
20	183.31±7.00	2	0.60	90-θ
Notes:				
1. Values from first flight model.				
2. The polarization angle is defined as the angle from horizontal polarization (i.e., electric field vector parallel to satellite track) where θ is the scan angle from nadir. In this table, the polarization angle is horizontal when the angle indicated is θ and vertical when 90-θ.				

Table 5. AMSR-E Channel Characteristics (From http://www.ghcc.msfc.nasa.gov/AMSR/)						
CENTER FREQUENCIES (GHz)	6.925	10.65	18.7	23.8	36.5	89.0
BANDWIDTH (MHz)	350	100	200	400	1000	3000
SENSITIVITY (K)	0.3	0.6	0.6	0.6	0.6	1.1
MEAN SPATIAL RESOLUTION (km)	56	38	21	24	12	5.4

B. ADVANCED MICROWAVE SCANNING RADIOMETER FOR (EOS)

The Aqua Advanced Microwave Scanning Radiometer for EOS (AMSR-E) is a multiple frequency band radio sensor that measures faint radio waves radiated from the earth surface and atmosphere. This radiometer measures polarized radiance (vertical and horizontal) in six frequency bands from 6.9 GHz to 89 GHz (Table 5).

The instrument scans counterclockwise in a conical manner at a 10 km sampling interval. The instrument accomplishes a complete revolution in a period of 2.6 msec and samples radiances with a period 1.3 msec. The scan geometry corresponds to an observing swath width of about 1450 km. The aperture diameter of the AMSR-E antenna produces a spatial resolution of about 5 km in the 89 GHz band; 15 km in the 36.5 GHz band; 25 km in the 18.7 and 23.8 GHz bands; and 50 km in the 6.9 and 10.65 GHz bands. These bands are used in various algorithms to estimate water vapor, cloud liquid water, amount of precipitation, sea surface wind, sea surface temperature, ice concentration, and snow water equivalent.

III. DATA

Numerical model and infrared (IR), visible, and WV imagery are the primary tools employed operationally to forecast TC intensities and ETs. The techniques derived from these tools, however, are far from perfect. Models and short/middle wavelength satellite data intensity calculations often over or under estimated the ET process (Jones et al. 2003).

A. INTENSITY ESTIMATING TOOLS

1. Limitations of Numerical Forecast Models

Jones et al. (2003) stated, "The relatively small scale of the tropical cyclone and the complex physical processes that occur during the interactions between a tropical cyclone and the midlatitude environment present difficult numerical forecast problems." Furthermore, the degradation of model forecast skill, as a result of an ET event has been shown to extend across an entire ocean basin. In their study of the ET of Typhoon Joy, Typhoon Kirk, and Typhoon Orson in August 1996 using the Navy Operational Global Atmospheric Prediction System (NOGAPS) model, Jones et al. (2003) found that large location and intensity errors resulted during the re-intensification of the decaying tropical cyclone.

Jones et al. (2003) identified large variability in the representation of an ET event by different sets of forecasts that are initialized from sequential analyses as a characteristic associated with the numerical prediction. They compared observational data to the Japan Meteorological Agency model forecast of Typhoon Bart (1999) and found that the forecasted central sea-level pressures

were consistently deeper than the verifying analysis values during the intensification and weakening stages of the ET. However, when they compared the NOGAPS forecasts of the ET of Typhoon David (1997) to observations, they found that the forecast did not deepen the extratropical system enough.

They concluded that the numerical forecast errors were highly dependent on the initial conditions. The uncertainty in the initial conditions is partly a result of bogusing (DeMaria et al. 1992; Kurihara et al. 1993; Heming and Radford 1998; Davidson and Weber 2000; Pu and Braun 2001) the tropical storm vortex. The bogusing process of the model may delay the onset of ET. Another significant contributor to uncertainty is the unavailability of satellite data for assimilation into the initial conditions.

2. Limitations of IR and Visible Imagery

The enhanced Dvorak method (Dvorak 1984), which uses visible and infrared satellite imagery to observe storm center of rotation, prominent cloud features, and cloud-top features, is most commonly used to estimate TC intensity. The main limitation of the Dvorak method is that it is subjective rather than objective. Dense cloud cover can obstruct the view of the storm center, which increases the potential for forecasters to inaccurately place the storm center location.

The Dvorak method is based on the presumption that certain cloud structures and locations are signs of intensity and intensity change. The major inadequacy of the Dvorak method (cloud cover in the vicinity of TCs) limits the retrieval of physical parameters associated with

TC intensity. This is now being overcome with the use of microwave imagery.

3. Limitations of Microwave Imagery

Microwave satellite sensors measure radiances emitted from the earth's atmosphere, clouds, and surface. Microwave wavelengths are significantly longer than visible and infrared portions of the spectrum. The retrieval of earth-emitted radiances at such long wavelengths requires large antennas and the low energy levels necessitate the deployment of the sensors on low altitude, polar-orbiting spacecraft.

The polar-orbiting satellite provides global microwave coverage of the earth's atmosphere and surface every 12 hours. During this period, the satellite makes approximately 14 ascending and descending passes. A pass (swath) is referred to as ascending when the satellite travels from south to north and descending when the satellite travels from north to south.

Because polar satellite overpass times and locations are variable, significant temporal and spatial resolution challenges result. When the orbits overlap, multiple satellite composites can provide information for relatively large regions. The extent of the region is highly dependent on the extent of the overlap coverage. If the swath width is large enough, coverage gaps are minimal. Conversely, narrow swath orbits can lead to large gaps in data from one swath to the next. These data gaps along with the instrument's scan geometry may make it a less than optimal analysis tool.

The small swath size and temporal and spatial resolution of the data are a direct result of the

instrument's scan geometry. The cross-track-scanning AMSU swaths are nearly 2200 km wide. Demuth (2004) noted that due to instrument geometry, however, the samples she used were limited to those cases in which the storm center fell within 600 km of the swath center, which limited the data resolution to approximately 50-80 km.

Brueske (2003) calculated TC MSLP using AMSU-A imagery and found that his algorithm was sensitive to the size of the storm's eye. This highlighted the challenges associated with AMSU's low data resolution. He found that storms with an eye considerably less than 48 km in diameter resulted in underestimations of MSLP. Therefore, in such cases, eye size information was augmented with data from the Automated Tropical Cyclone Forecast package to improve the performance of the retrieval algorithm.

The mesoscale properties of a TC make microwave sampling of the storm difficult in most cases. The synoptic-scale nature of the ET process, however, does not present the same spatial resolution problems. Utilizing microwave imagery with a synoptic-scale approach (100-1000 km) does not require the storm to fall within the swath center. With this approach, the evolution of the environment in the vicinity of the TC becomes as important as the evolution of the TC. A synoptic-scale approach allows for the retrieval of useful TC information even when the storm center is located in a data gap.

B. DATA PROCESSING

AMSU-A data were obtained from the Cooperative Institute for Research in the Atmosphere (CIRA) at <http://amsu.cira.colostate.edu/>. The AMSU-B and AMSR-E data were supplied by the Naval Research Laboratory,

Monterey. The NOGAPS data were provided by the Fleet Numerical Meteorology and Oceanography Center, Monterey. All data were interpolated to a common 50 km grid centered at 130E 40N. However, AMSU-A data required additional processing prior to the grid construction.

1. AMSU-A Temperature Measurement

Once the temperature profile is retrieved, the hydrostatic equation can be used to determine the minimum sea level pressure (MSLP). Demuth (2004) accomplished this by using normalized radiances (collected for storms in Atlantic and east Pacific basins during the 1999–2001 tropical-cyclone seasons) as input to a statistical temperature retrieval to determine atmospheric pressure. Although 40 levels from 1000 to 0.1hPa were available, only standard levels, between 920 and 30hPa, were used. Since surface pressure cannot be derived from AMSU data, it was taken from the National Centers for Environmental Prediction global analysis. The hydrostatic equation was again used to integrate surface pressure up to the minimum AMSU derived pressure.

Brueske (2003) noted, “Measurements (55-GHz region) of TC upper-tropospheric warm anomalies (UTWAs) are linked to either surface wind structure or MSLP using thermodynamic and dynamic constraints on the TC scale (i.e., several hundred kilometers).” To establish this relationship, he developed the following regression equations:

$$MSLP_{ret} = (150.7 - \delta B_{ret}) / .15 \quad (3.1)$$

$$MSLP_{raw} = (65.4 - \delta B_{raw}) / .07 \quad (3.2)$$

where B_{ret} is the retrieved brightness estimate derived from limb-corrected AMSU-A 54.94 GHz brightness temperature data

and B_{raw} is the raw 54.94 Ghz brightness temperature data. The regression coefficients are based on a sample size of 53 storms from the 1999 and 2000 seasons. Tests of the algorithm revealed that there is a linear correlation between UTWAs and reconnaissance estimates of MSLP.

2. AMSU-A Antenna Correction

Radiance measurements for AMSU-A are performed between 48° off nadir at 30 scan angles or positions. The majority of the radiance retrieved by the antenna (~95%) is received via the main beam and the remaining portion (~5%) is received via the side lobes (Mo 1999). The side lobes, which receive contributions from the satellite and space, necessitate an antenna adjustment. Equation 3.3, developed by Mo (1999), is used to convert the raw antenna temperature to brightness temperature:

$$T_A(\beta) = \frac{1}{N_\eta} \left[f_e(\beta) \bar{T}_E + f_c(\beta) \bar{T}_C + \eta f_{\text{sat}}(\beta) \bar{T}_{\text{Sat}} \right] \quad (3.3)$$

$$N_\eta = f_e(\beta) + f_c(\beta) + \eta f_{\text{sat}} \quad (3.4)$$

where T_A is the antenna temperature, T_E is the temperature of the earth (brightness temperature), T_C is the temperature of cold space, T_{sat} is the temperature of the satellite, $f_e/f_c/f_{\text{sat}}$ are the antenna frequencies of the earth, cold space and the satellite respectively, and β is the scan angle. In calculating T_E in equation 3.8, we must assume that T_C is a constant 2.73 K and the T_{sat} term is negligible because its maximum contribution is of the order of .001 K.

Prior to antenna corrections, limb corrections must be made to the radiance values. A limb correction is made to compensate for the variation in radiance retrieved from the

earth due to differences in beam position and varying optical path length.

3. AMSU-A Limb Correction

Making adjustments to AMSU data to correct limb error has been derived by physical, statistical, or a combination of physical and statistical approaches (Goldberg et al. 2001). Goldberg et al (2001) found that asymmetries in the nadir weighting functions made the use of a purely physical approach impractical. Limb corrections in this study were based on a statistical algorithm provided by the Cooperative Institute for Meteorological Satellite Studies (Woolf, personal communication).

THIS PAGE INTENTIONALLY LEFT BLANK

IV. RESULTS

In this case study, analysis and diagnostics center on two October 2004 western North Pacific TCs, Tokage and Ma-on. Examination starts when Tokage and Ma-on entered the transformation stage (Klein et al. 2000). The examination period is 42h for each TC. This is based on the study of Klein et al. (2000) in which it was shown that once transformation begins, TCs generally complete ET within 42 h.

Examination began with a synoptic overview. Infrared satellite imagery and WV imagery were used to identify cloud and moisture features of the TC environment. Also, NOGAPS 0000 UTC and 1200 UTC analysis were used to examine TC structure and dynamics as compared to IR and WV imagery. Analyzed fields of 500 hPa heights, 200 hPa winds and 500 hPa omega were used to compute various diagnostics and to identify several features that aided or inhibited the TC throughout the ET period. Because 0600 UTC and 1800 UTC analyzed fields were not available, 6-h forecasts from the 0000 UTC model run and 1200 UTC model run were used to provide a 6 h time resolution. When available, microwave data were used in conjunction with model-based diagnostics to complete the analysis of the ET processes for both cases.

Diagnosis of the TC transition was accomplished using the Petterssen Frontogenesis Function (Keyser 1988)

$$F = \frac{d}{dt} |\nabla \theta| = \frac{1}{2} |\nabla \theta| (E \cos 2\beta - \nabla \cdot \mathbf{v}) \quad (4.1)$$

$$E = E_{st}^2 + E_{sh}^2 \quad (4.2)$$

where E is the sum of the stretching and shearing deformation and β is the angle between the axis of dilatation and the isentropes. Resolving F into natural coordinates (s,n) yields

$$F = F_n n + F_s s \quad (4.3)$$

Here the coordinate s is locally tangent to an isentrope and the coordinate n is normal to the isentrope and points in the direction opposite to $|\nabla\theta|$ (i.e., toward colder air). The vector F_n is labeled scalar frontogenesis as it defines the magnitude of the change in $\nabla\theta$. The distribution of F_n will be concentrated where confluence/diffluence patterns, which are defined by the movement of the decaying TC circulation into the midlatitude westerlies, acts to change $|\nabla\theta|$. The vector F_s is labeled rotational frontogenesis and defines the change in the direction of $\nabla\theta$. The distribution of F_s will be concentrated where the rotation of the decaying tropical cyclone is acting to build the thermal ridge and deepen the thermal trough. The evolution of F_n and F_s were examined after 18 h into the transformation stage with respect to the frontogenesis contributions to precipitation and water vapor transport as identified by microwave imagery.

Channel 7 of AMSU-A was used to resolve upper-level temperature structure over the decaying TC. Channel 18 of AMSU-B was used to resolve upper- and mid-level moisture gradient. However, AMSU-B imagery was limited to the early transformation stage and subsequently could not be used to identify or diagnose the critical re-intensification period. Precipitation based on AMSR-E was calculated from

an algorithm by Lui (2002) that uses 89 Ghz and 18.7 Ghz channels. The WV analysis was based on AMSR-E and was calculated by differences of the 23.8 Ghz and 18.7 Ghz channels. Although TC Ma-on occurred before TC Tokage, Ma-on failed to complete ET. Therefore, TC Tokage will be discussed first and the characteristics of Ma-on will be compared to Tokage

A. TOKAGE

1. Synoptic Overview

Tokage began its transformation south of Japan at 31N 132E at 0000 UTC 20 October (Figure 5). At this time, cold air advection (CAA) behind the TC and warm air advection (WAA) ahead of the TC began to produce an asymmetric deformation of the upper-level TC cloud structure. The large cloud shield seen on IR imagery (Figure 5a) indicated outflow into strong zonal flow north of the TC. The large subsidence and dry area northwest through southwest, as seen by the dark region in Figure 5b, was related to CAA. A moisture boundary south of the TC was characteristic of a midlatitude cold front and the upper-level outflow and the increased region of cloudiness to the northeast was indicative of a midlatitude warm front. A concentration of deep convective clouds was still identifiable near the center of the decaying TC.

The decaying TC continued to have a concentrated MSLP center (Figure 5c). A quasistationary primary midlatitude low was positioned to the northeast and the low-level subtropical ridge was positioned to the east. Two midlatitude shortwave troughs were propagating within the midlatitude westerlies. Vertical wind shear, due to the midlatitude westerlies, contributed to the reduced vertical

extent of the decaying TC such that an open wave was evident at 500 hPa (Figure 5c).

As Tokage began its transformation, it was located equatorward and to the rear of a 200 mb jet streak (Figure 5d). A strong couplet of subsidence to the north and upward vertical motion to the south of the entrance region of the jet streak was evident from the 500 mb omega chart. The location of the jet streak relative the TC produced a wide area of enhanced upward motion to the northeast of Tokage. The southern most region of upward motion matched well with the enhanced cloudy region associated with the decaying TC (Figure 5a). Ahead of the TC, WAA contributed to a second region of upward motion. This second minimum area was also enhanced by jet streak dynamics. The two distinct areas of maximum vertical motion revealed that Tokage lagged behind the area of peak jet streak-induced vertical motion.

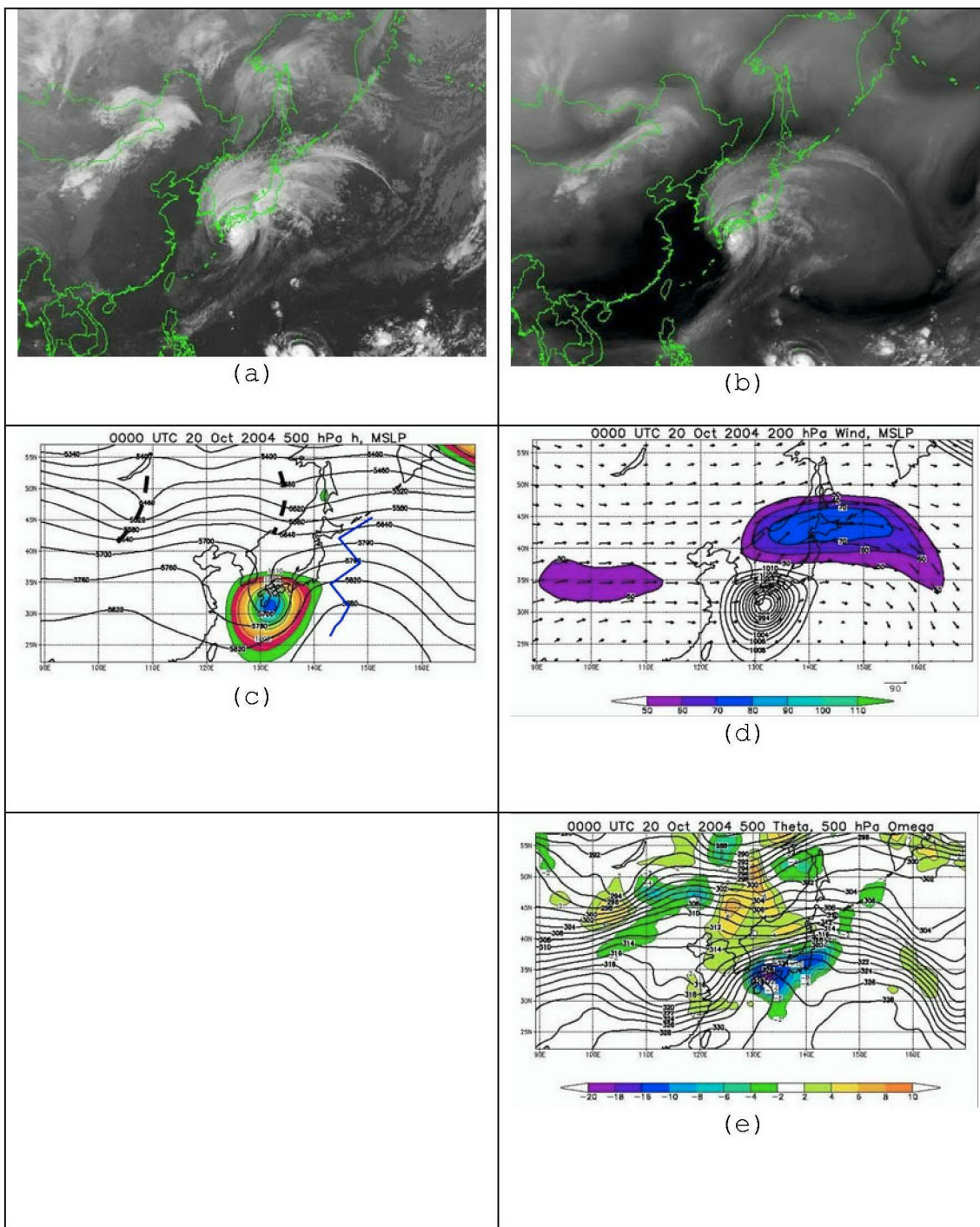


Figure 5. (a) IR and (b) WV imagery at 0000 UTC 20 Oct 2004; (c) 500 hPa height (m) and MSLP (hPa); (d) 200 hPa wind (m s^{-1}) and MSLP (hPa); and (e) 500 hPa potential temperature (K) and omega ($\mu\text{b s}^{-1}$). All gridded files are from the NOGAPS analysis at 0000 UTC 20 Oct 2004.

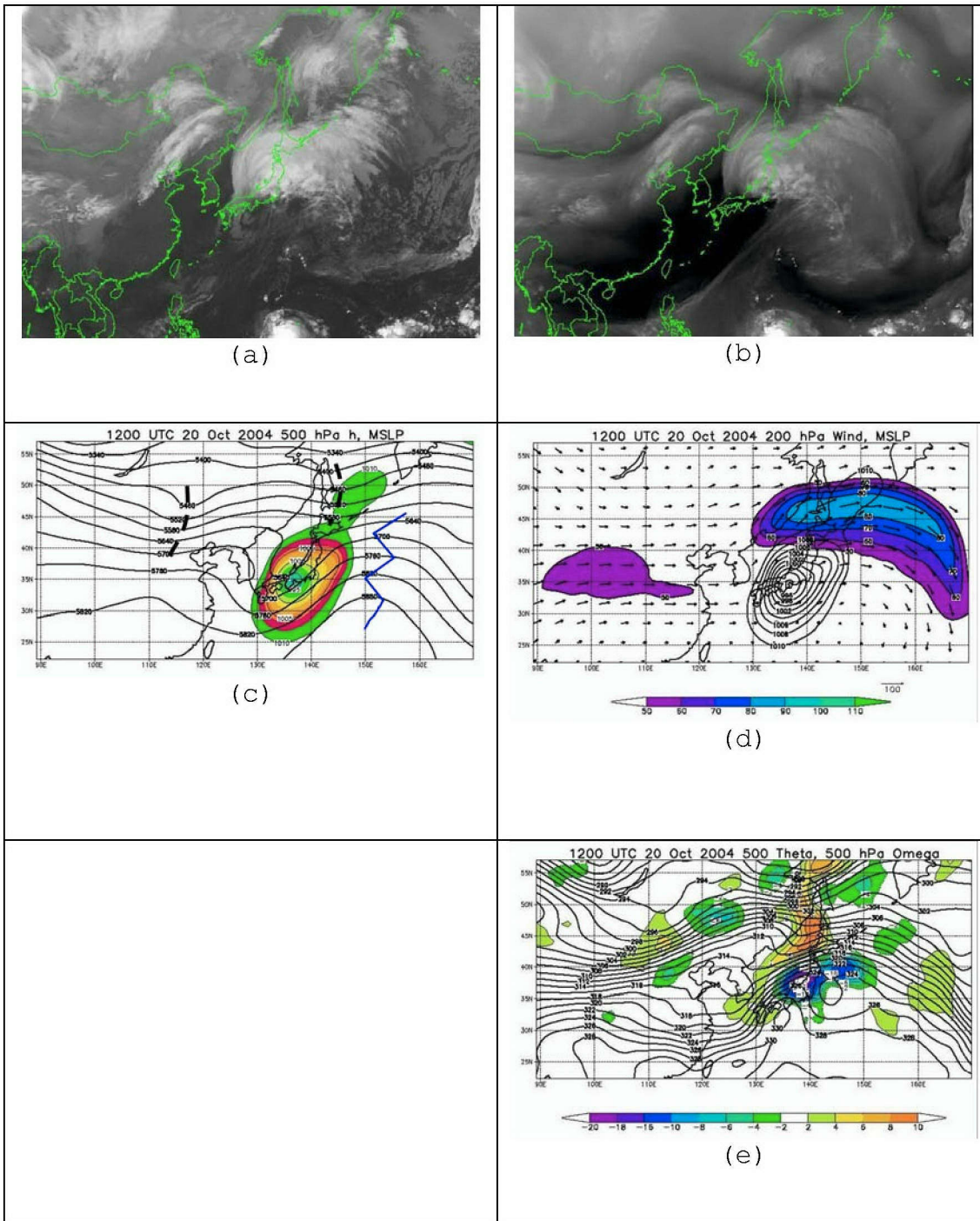


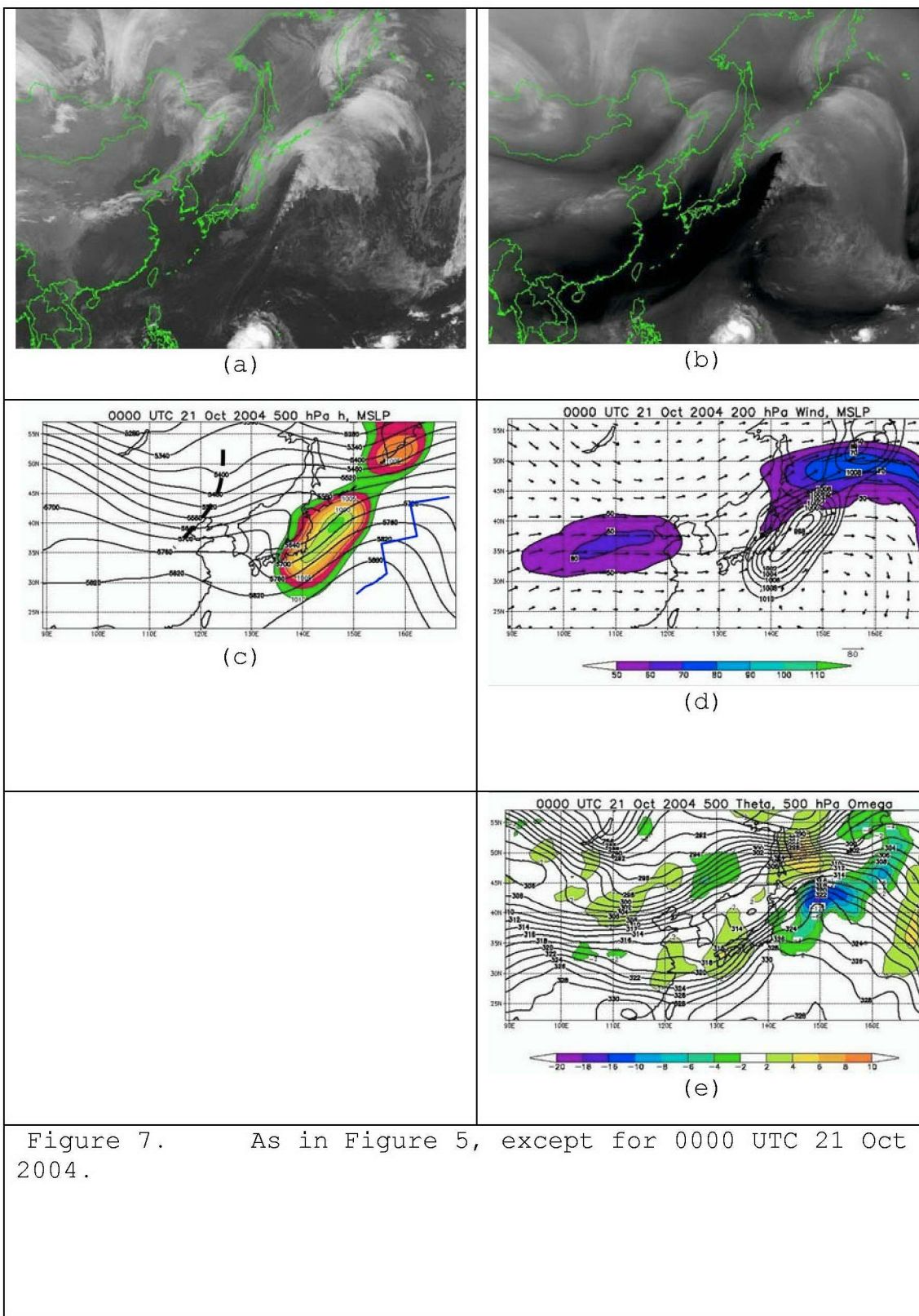
Figure 6. As in Figure 5, except for 1200 UTC 20 Oct 2004.

Tokage continued to decay as a TC over the next 12 h (Figure 6). The IR cloud signature over the TC center continued to decrease (Figure 6a) as subsidence began to erode the TC center (Figure 6b). Subsidence appeared to dominate the region south of the TC, but there was a notable increase in the horizontal extent of the clouds north of the center (Figure 6a). It appeared that the confluence of WAA to the east of the TC and westerly midlatitude flow to the north had begun to enhance the thermal gradient.

At 1200 UTC 20 Oct, the cyclone center at the surface had become elongated with a trough extending to the northeast and southwest (Figure 6c). The MSLP increased by 5 hPa. A secondary low-pressure system developed in advance of the 500 hPa trough north of the TC.

The jet streak at 200 hPa increased by 10 m s^{-1} and remained oriented in a zonal direction in the region of the TC (Figure 6d). The thermal ridge had begun to build to the east and the area of upward motion was expanding eastward (Figure 6e). The jet streak/midlatitude flow appeared to be moving east faster than the TC. AMSU-A data will be used at this point to resolve the TC thermal structure as it moved from the tropics to a midlatitude environment.

Tokage continued to decay through 0000 UTC 21 Oct (Figure 7). A closed upper-level circulation was no longer identifiable on IR imagery (Figure 7a). A dry tongue had developed between the eastern section of the cloud shield and the clouds that wrapped around the west side of the TC.



Two distinct areas of enhanced cloudiness had developed within the cloud shield and convection indicative of a cold front began to develop along the eastern border of the dry tongue.

The MSLP pattern associated with Tokage continued to become elongated and oriented northeast-southwest. Furthermore, the MSLP increased 9 hPa over the 24 h period between 0000 UTC 20 Oct and 0000 UTC 21 Oct (Figure 7c). There were no significant changes in the 500 hPa height pattern between 1200 UTC 20 Oct and 000 UTC 21 Oct.

Meridional flow from the upper-levels of the decaying TC contributed to a shift of the jet streak to the northeast (Figure 7d). The effect of the meridional flow on the jet streak could be seen in the southwest-northeast orientation of the isentropes west of the TC and the elongated omega pattern from 145E 35N to 165E 53N (Figure 7e). The two distinct areas of enhanced cloudiness seen on the IR imagery (Figure 7a) coincided with the omega minimum north of the thermal ridge and the jet induced omega minimum that had been displaced to the northeast. The distance between these features indicated that the TC was losing upper-level support. The increased theta gradient to the west and the fact that the TC had moved north of 30 deg latitude suggested that the TC was well into the transformation stage. The utility of AMSU-A data in analyzing the upper-level thermal gradient will be examined at this critical point of the ET process.

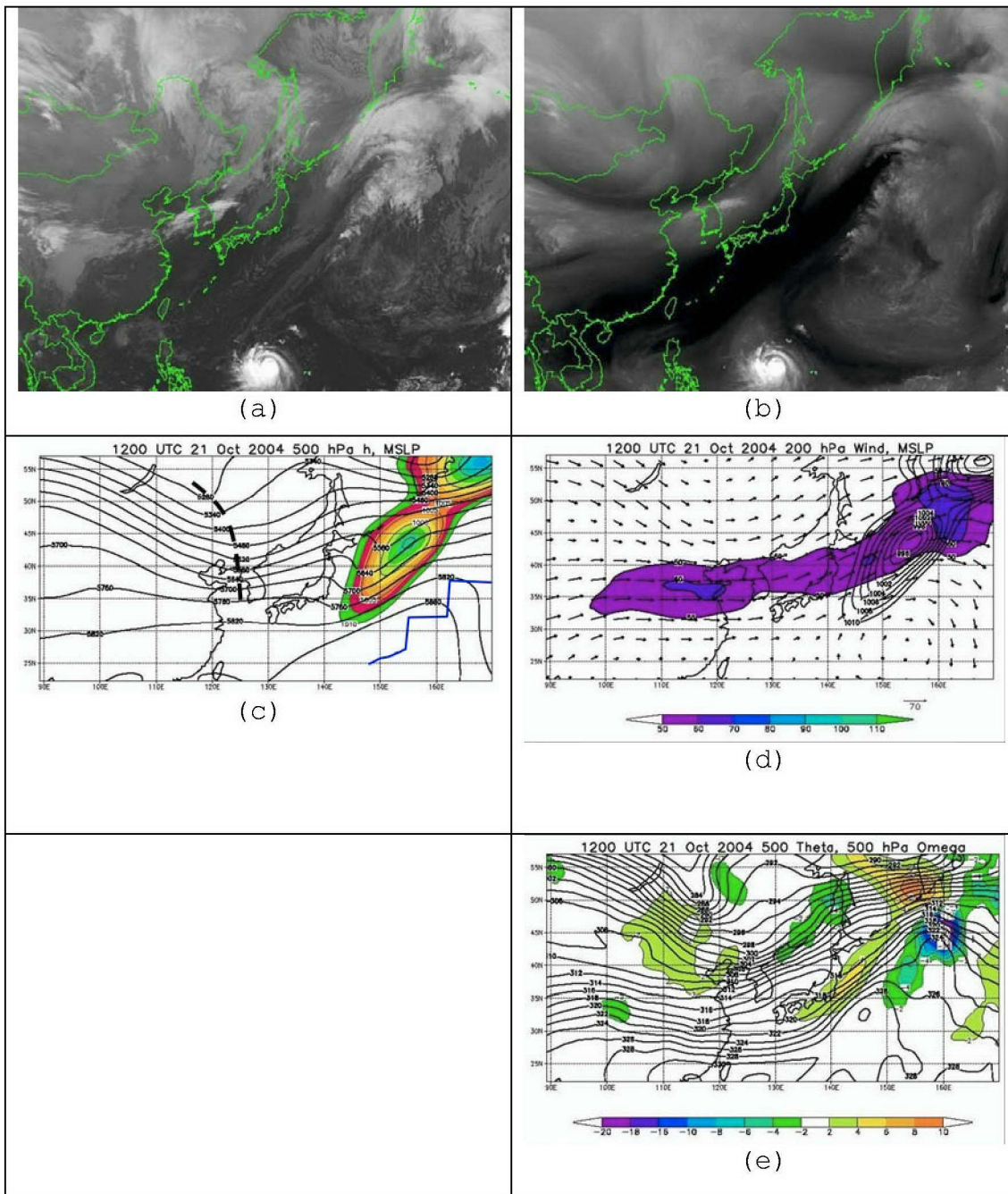


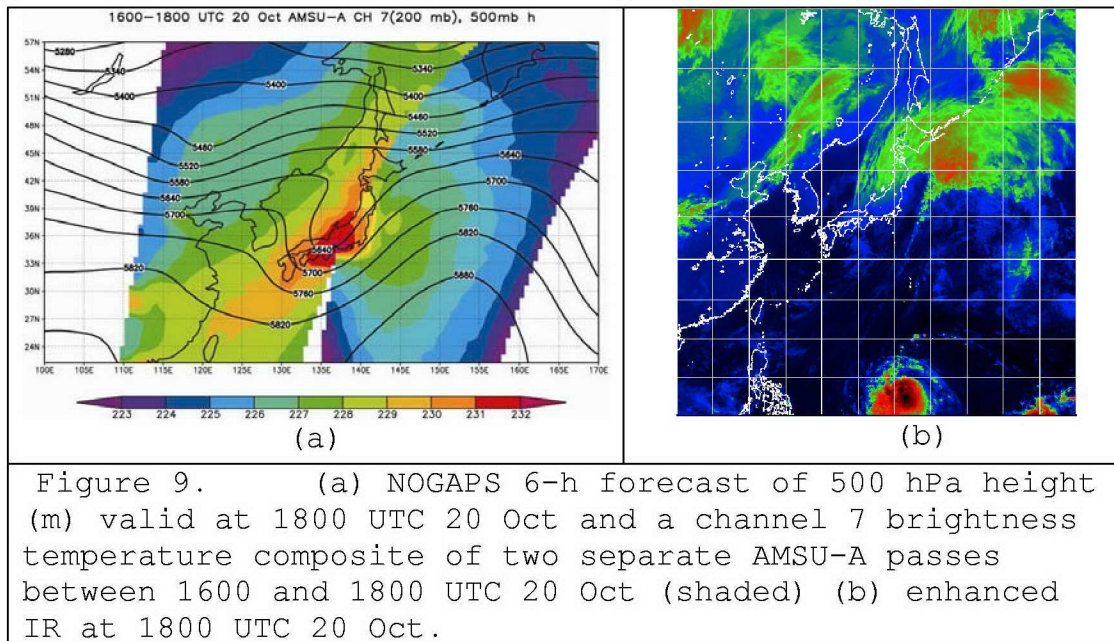
Figure 8. As in Figure 5, except for 1200 UTC 21 Oct 2004.

After 36 hours into the transformation stage (Figure 8a), Tokage had entered the re-intensification stage and the MSLP began to decrease. Low-level asymmetry had become evident in the development of a low-level moisture boundary south of the TC center (Figure 8a). Although the MSLP had lowered, the 500 hPa trough above the TC had begun to fill and the zonal flow (now oriented southwest-northeast) and the 200 hPa jet streak weakened. A remnant of the jet streak remained between the midlatitude low to the northeast and the low-level circulation associated with the remnants of Tokage. However, the jet orientation, the 500 hPa thermal gradient west of the TC, and the 500 hPa thermal ridge north of the TC were midlatitude features. Increased CAA behind the TC and jet streak divergence ahead of the decaying TC (along with WAA) contributed to a reduction of the MSLP and increased the vertical motion poleward of the thermal ridge. At this stage, Tokage now had more frontal characteristics representative of an extratropical cyclone.

2. Diagnostics

The availability of microwave data facilitated its use in estimating the extratropical transition process at 1800 UTC 20 Oct. The upper-level structure of the TC was determined using AMSU-A imagery (Figure 9) as it moved into the subtropical environment. A 6-h 500 hPa height forecast valid at 1800 UTC 20 Oct and a composite of two AMSU-A (channel 7) satellite passes (Figure 9) provided a view of Tokage's structure as it began the transformation process. Channel 7 was chosen for this analysis because it provides a measure of the upper-tropospheric temperature structure (Figure 3) above the decaying TC. The red area centered at 138E 33N was co-located with the TC center, which indicated

that the TC continued to maintain its warm vertical structure. A second area of interest was the warm area marked by dark green shading centered at 145E 36N. When compared to IR imagery (Figure 9b), it was noted that the primary cloud areas occur along the northern border of this region (Figure 9b). Attention focused primarily on these two regions during the diagnosis of frontogenesis during the TC transition process.



The AMSR-E derived rain areas (Figure 10) coincide with areas of upward motion and enhanced cloudiness seen in Figure 9. Note that precipitation is not derivable over land areas. At 850 hPa, the scalar vectors (F_n) (Figure 10b) were concentrated poleward of the thermal ridge and equatorward of the AMSR-E calculated precipitation. The rotational vectors (F_s) (Figure 10a), were concentrated west of the thermal ridge and extended south to the TC center. Forcing of vertical motion due to scalar and rotational frontogenesis is defined by the divergence of

the two frontogenesis vectors, respectively. The scalar and rotation divergence contributions at 850 hPa were identified in the precipitation region and near the TC such that the scalar component was most significant north of the ridge and the rotational component dominated the TC region.

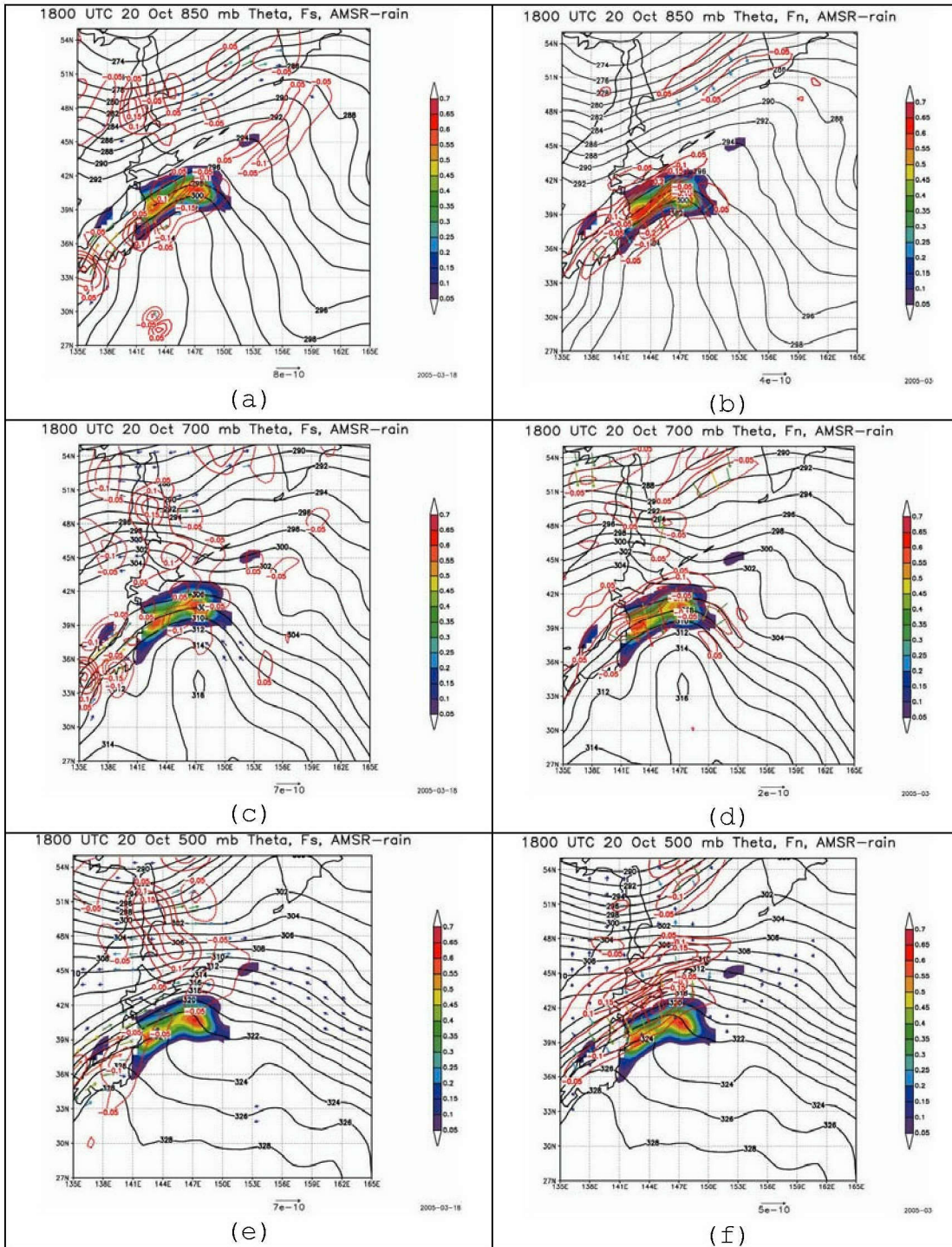
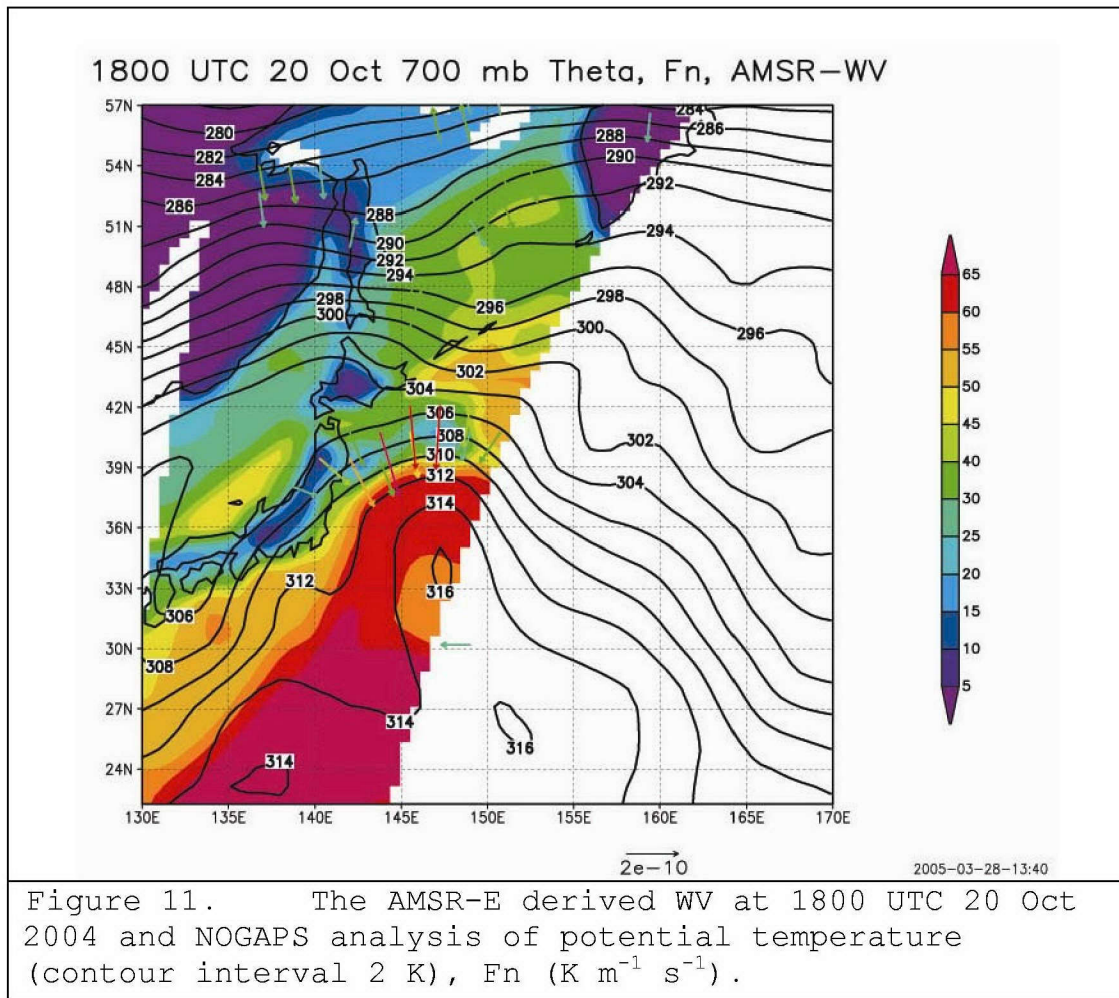


Figure 10. Analyzed potential temperature (K) and F_s vectors (left column) and F_n vectors (right column) at 850 hPa (top row), 700 hPa (middle row), and 500 hPa (bottom row) for 1800 UTC 20 Oct 2004. Vector magnitudes are defined by the scale vector in the lower right of each panel. Units are $K m^{-1} s^{-1}$. Contours define the divergence of F_n and F_s vectors and are units of $\mu b s^{-1}$. Shaded regions are AMSR-E derived rain

Scalar frontogenesis and its associated contribution to vertical motion remained strong in the region north of the ridge and was concentrated directly over the precipitation region at 700 hPa (Figure 10d) and across the WV gradient north of the ridge (Figure 11). The configuration of the AMSR-E WV along the 700 hPa isentropes with the max WV over Tokage provided a measure of the environmental WV gradient due to warm moist air moving poleward east of Tokage and cooler dry air moving southward west of Tokage. The rotational vectors at this level were concentrated on both sides of the thermal ridge. This indicated that the ridge was building south of the precipitation area (Harr et al 2000). The vertical motion in the region near the TC was dominated by forcing from rotational frontogenesis.

The scalar vectors were equatorward of the AMSR-E precipitation at 850 hPa, over the precipitation at 700 hPa, and poleward of the precipitation at 500 hPa (Figure 10e). From this, it was determined that the warm-front ahead of the TC tilted to the northwest in the vertical. The 500 hPa rotational vectors remained concentrated to the west of the thermal ridge and sustained forcing of vertical motion in the region of the TC (Figure 10f). The 500 hPa concentration of rotational vectors to the east of the thermal ridge was located north of those seen at 700 hPa (Figure 10e), which indicated a building of the ridge north of the TC at this level. Hence, rotational vector divergence poleward of the precipitation was associated with the 500 hPa trough northeast of the TC.



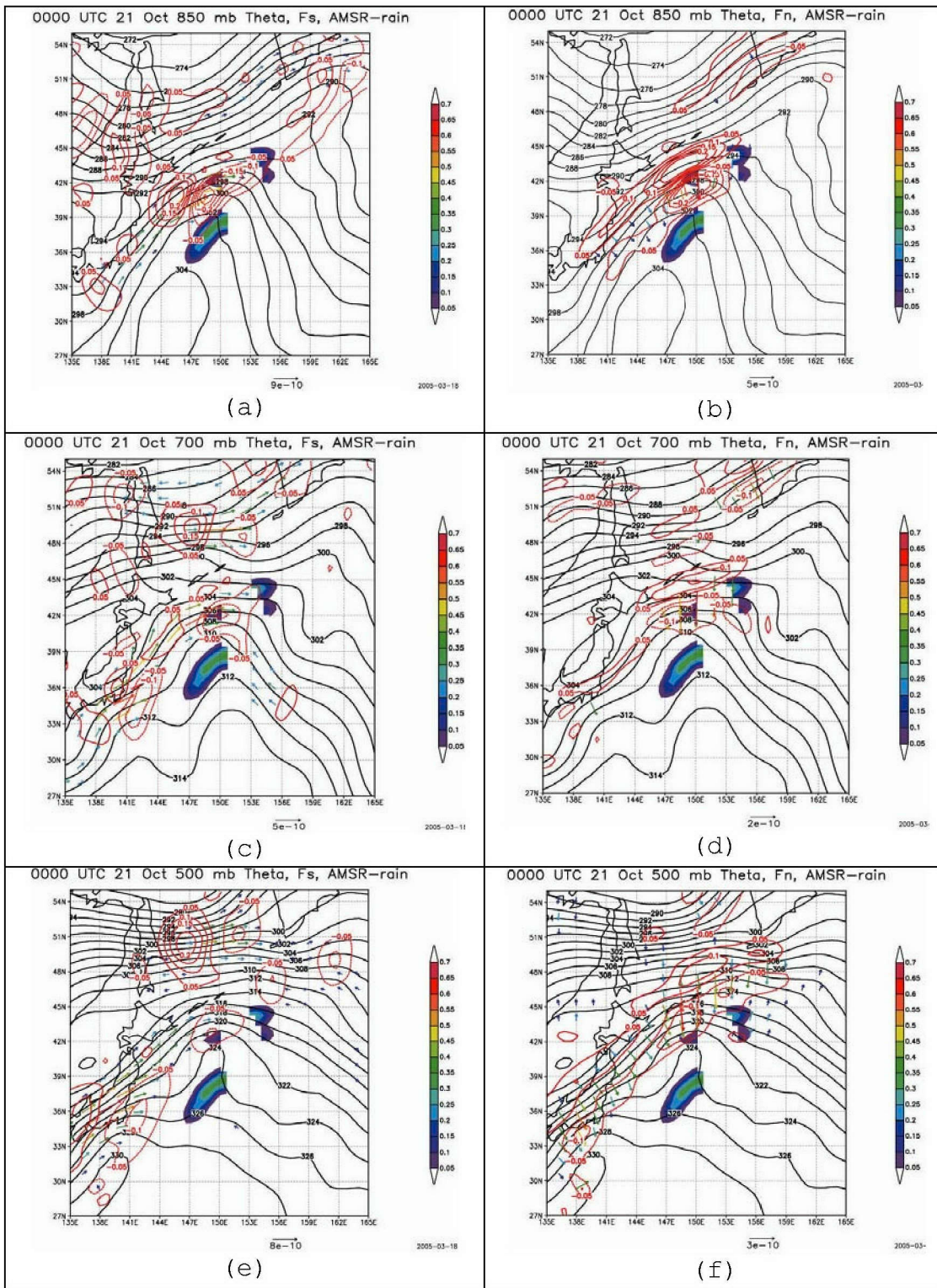
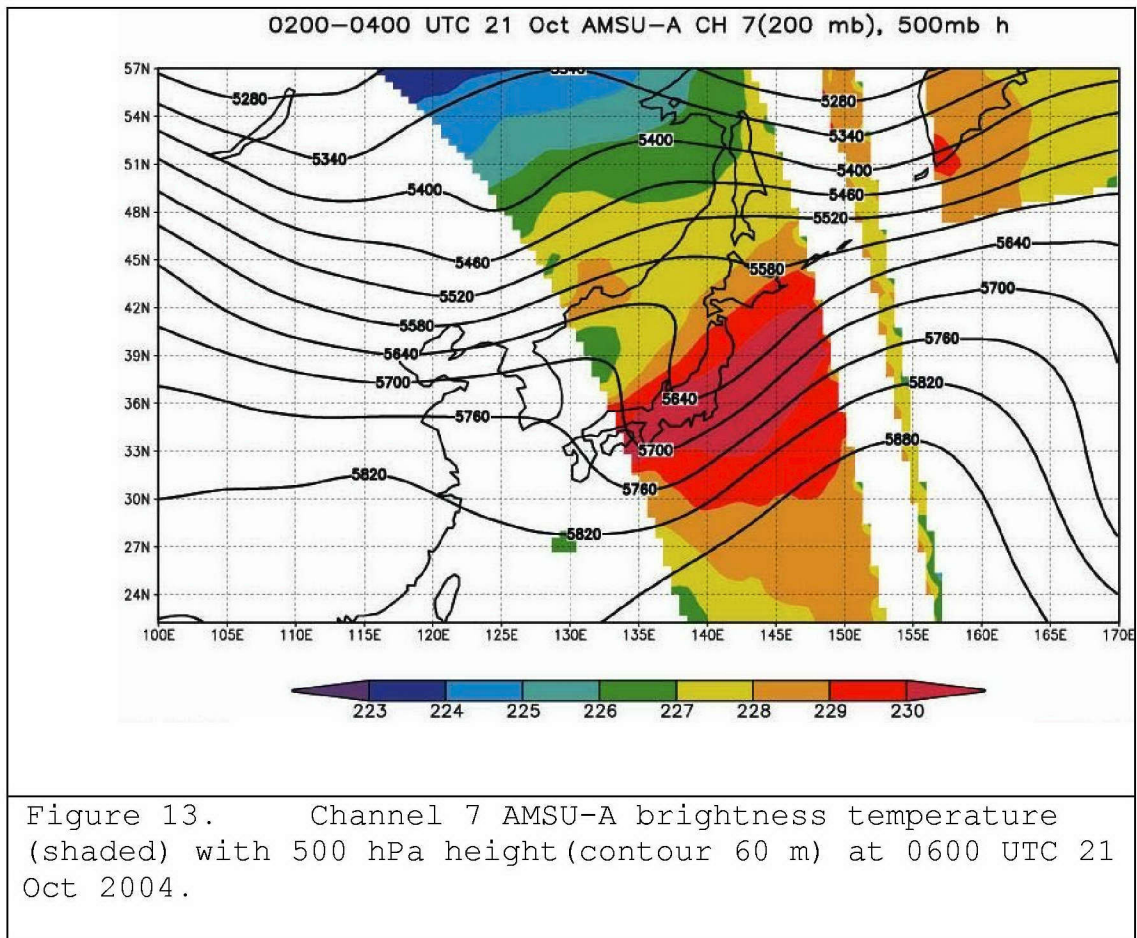


Figure 12. As in Figure 10, except for 0000 UTC 21 Oct 2004.

Twenty-four hours into the transformation, Tokage continued to be located west of the low-level thermal ridge. Therefore, the 850 hPa concentrations of scalar and rotational vectors were both located equatorward of the primary AMSR-E derived precipitation and extended southward west of the thermal ridge (Figures 12a,b). In both cases, the maximum forcing of upward motion was located in the region south of the AMSR-E precipitation.



As in Figure 10, the scalar frontogenesis vector was equatorward of the precipitation region at 850 hPa (Figure 12b), within the region at 700 hPa (Figure 12d), and poleward of the region at 500 hPa (Figure 12f). A significant change was observed in the 500 hPa scalar vector concentration. The vector concentration at 500 hPa

spread over a broad region west of the thermal ridge. This was evidence that synoptic-scale dynamics had begun to affect the ET process.

The AMSR-E derived WV imagery (Figure 11) indicated an increase in moisture within the thermal ridge at the TC center. The potential temperature gradient along the thermal ridge was oriented parallel to the WV gradient (Figure 11). In addition, the 700 hPa scalar vector concentration was located at the top of the thermal ridge where the strongest WV gradient was located.

The rotational frontogenesis vector concentration at 850 hPa remained west of the thermal ridge (Figure 12a). The maximum rotational forced divergence shifted north and east as the TC continued to move into the midlatitudes. At 700 hPa (Figure 12c), the vector concentrations on both sides of the thermal ridge increased and the maximum rotation forced upward motion west of the TC decreased from the 1800 UTC Oct diagnostic (Figure 10c). No significant changes occurred in the 500 hPa rotational vectors and associated upward vertical motion between 1800 UTC 20 Oct and 0000 UTC 21 Oct.

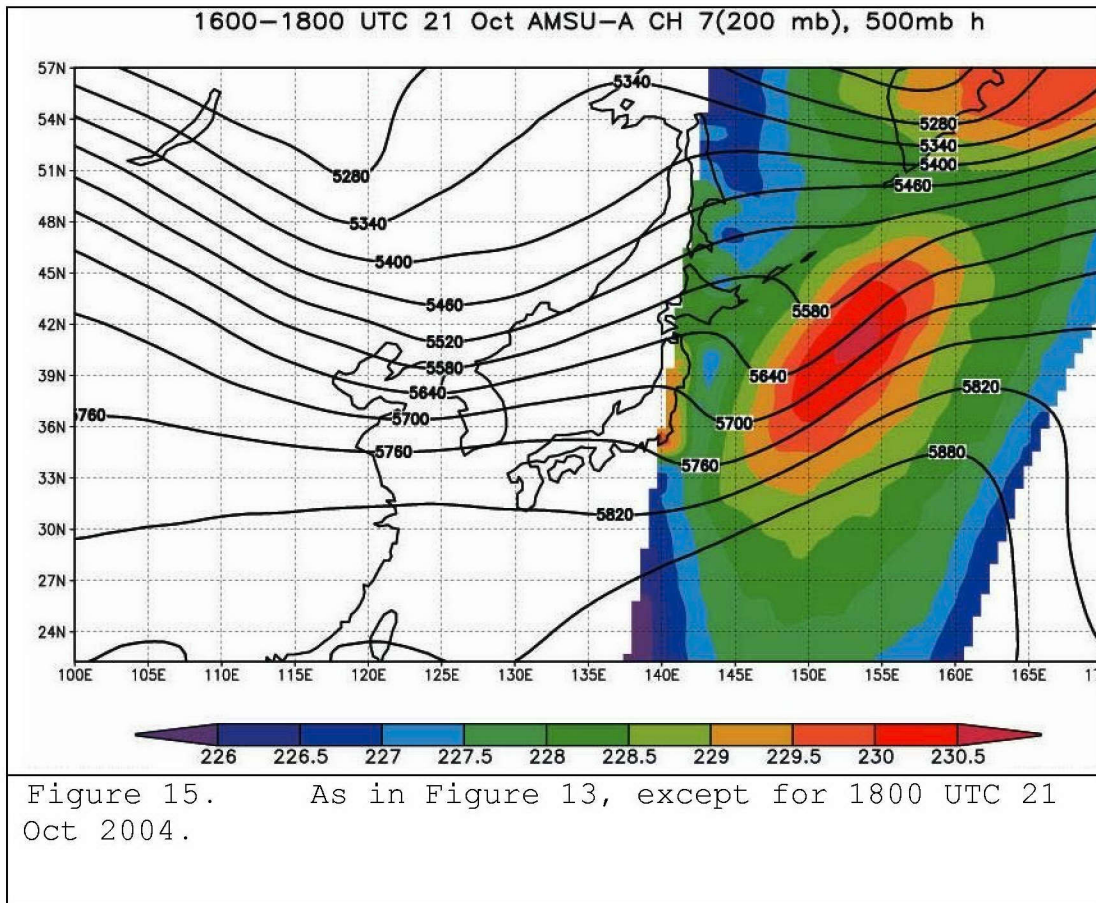
Over the ensuing 6 h, the TC warm-core signature could be identified in the AMSU-A imagery (Figure 13). Apparently, the upper-level warm area is being advected downstream by the midlatitude westerly flow. An additional upper-level warm-core signature was found just off the northeastern edge of the image. The temperature of this warm signature, associated with the midlatitude low, was approximately 230 K (the standard atmospheric temperature of the tropopause) and signified that undulation of the tropopause could be identified via AMSU-A imagery.

By 1200 UTC 21 Oct, the scalar vectors at 850 hPa were concentrated northeast and southwest of the AMSR-E derived maximum precipitation region (Figure 14b) and the associated upward motion was located along the thermal ridge axis. At 700 hPa (Figure 14d), the concentration of vectors was within the AMSR-E derived precipitation and the scalar contributions to vertical motion maximums were located above the 850 hPa concentration of vectors to the northeast and southwest. The 500 hPa scalar vectors remained concentrated west of the thermal ridge.

The rotational vectors were concentrated west of the thermal ridge axis at 850 hPa (Figure 14a). As with the scalar vectors, the rotational contribution to upward motion was oriented along the thermal ridge axis. However the magnitude of the rotational vector was larger than the magnitude of the scalar frontogenesis vectors. At 700 hPa, the rotational vectors were again concentrated on both sides of the thermal ridge (Figure 14c). The maximum rotational contribution to upward motion had shifted from the base of the thermal ridge to the top and increased in magnitude between 0000 UTC Oct (Figure 12c) and 1200 UTC Oct (Figure 14c). At 500 hPa (Figure 14e), both the rotational and scalar components exhibited synoptic-scale patterns. These synoptic-scale patterns coincided with the building of the mid-level thermal ridge as Tokage neared re-intensification.

The AMSU-A imagery at 1800 UTC 21 Oct (Figure 15) indicated that the upper-level warm-area was more symmetric than the warm-core above the TC at 0600 UTC 21 Oct (Figure 13). Because the remnants of Tokage had begun to re-intensify, the warm area on channel 7 AMSU-A imagery was

most likely a representation of the warm air above the tropopause that lowered over the developing extratropical cyclone.



In summary, Tokage began transformation at 0000 UTC 20 Oct 2004 as it moved into the midlatitudes. Upper-level jet streak dynamics and speed divergence that were evident in satellite imagery and the 500 hPa omega fields early in the transformation helped to couple the decaying TC with midlatitude flow. The asymmetric pattern associated with ET began in the upper-levels with the development of an outflow cloud shield to the north-east of the TC. The midlatitude westerlies also contributed to the reduced

vertical extent of the TC. However, the TC remained symmetric at the low-levels.

As the TC moved further into the transformation process, the upper- and mid-level structure continued to show signs of decay. Imagery from AMSU-A imagery provided evidence that the upper-level TC warm-core was being advected downstream by the midlatitude flow. Scalar and rotational patterns of frontogenesis and their associated upward vertical motion were used to evaluate relative contributions due to the TC remnant circulation and the confluence caused by the movement of the cyclone center into the midlatitudes. These diagnostics indicated that low- and mid-level asymmetries that developed were due in large part to confluence to the northeast of the TC and vorticity in proximity of the TC.

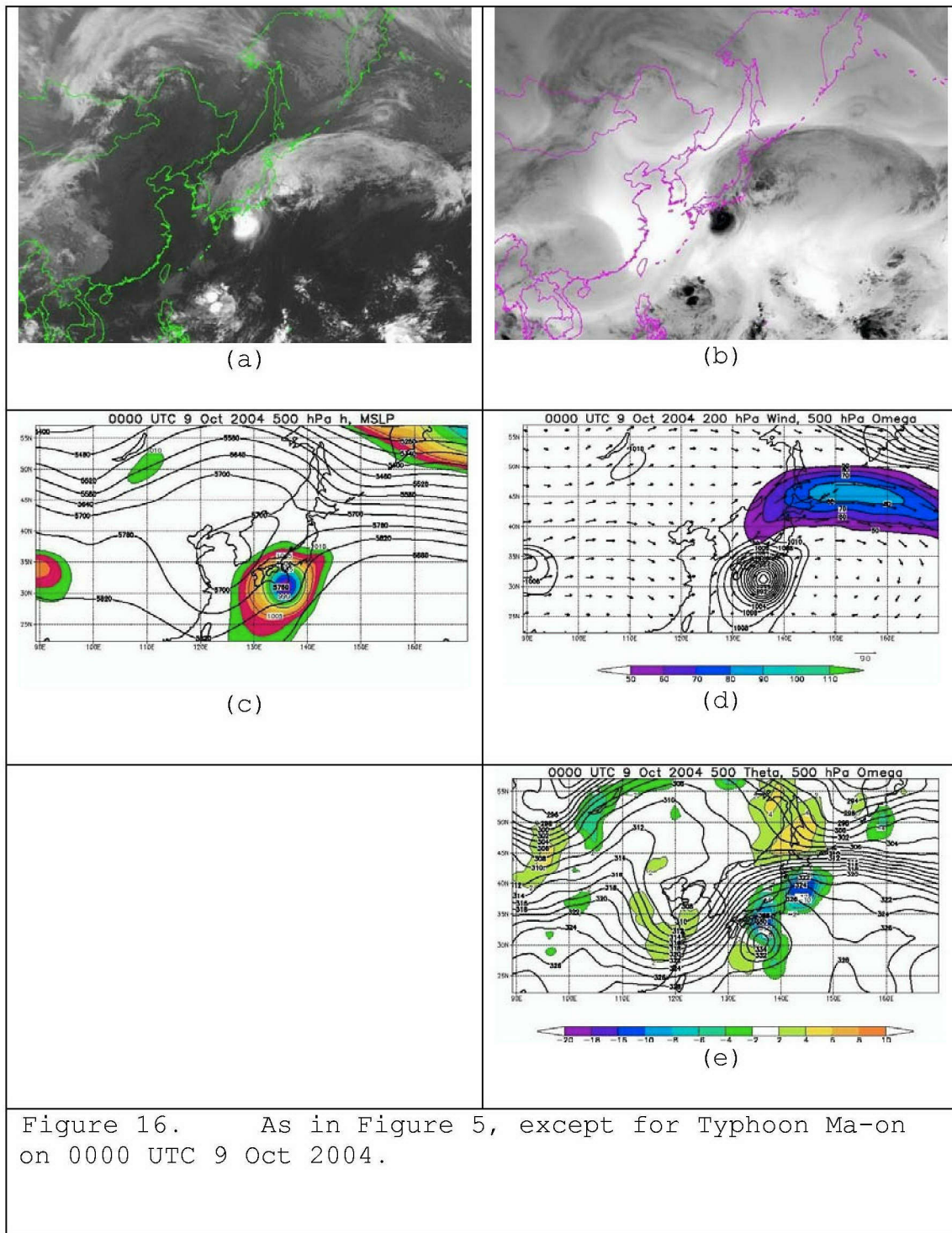
In addition, AMSU-A data contributed to the identification of changes in the upper-level warm region above the decaying TC. AMSR-E derived precipitation patterns and WV distributions identified that the scalar frontogenesis was responsible for the primary area of rainfall at the top of the thermal ridge. While the NOGAPS analyzed potential temperature distribution identified the extent and orientation of the thermal ridge east of Tokage. The AMSR-E derived WV revealed that the thermal ridge was more moist than its surroundings. This moisture was a source for the rainfall pattern over regions of scalar frontogenesis derived upward motion.

B. MA-ON

The evaluation of Typhoon Ma-on, which did not complete transformation, will now be compared with the ET of Typhoon Tokage.

1. Synoptic Overview

Examination of the transformation of Ma-on began at 0000 UTC 9 October (Figure 16) when the TC was located south of Japan at 32N 136E. A rather symmetric cloud pattern was evident in IR imagery (Figure 16a). The large cloud shield that extended north-northeast indicated that the upper-level outflow was being blown downstream by strong midlatitude zonal flow. Also noted was an area of strong vertical motion to the northeast of the TC (Figure 16e) along the southern border of the cloud shield (Figure 16b).



A symmetric cyclone center existed at the low-levels (Figure 16c) and a weak trough extended to the northeast and southwest of the TC center. A quasistationary primary midlatitude low was located to the northeast. The

subtropical high was positioned to the east. A 500 hPa midlatitude low was to the northwest and a midlatitude ridge was situated to the north (Figure 16c). Vertical wind shear, due to midlatitude westerlies, contributed to the reduced vertical extent of the decaying TC such that an open wave was evident at 500 hPa (Figure 16c).

Similar to Tokage, Ma-on began its transformation positioned in the divergent, entrance region of a zonal jet streak (Figure 16d). The 200 hPa jet streak in Figure 16d was closely aligned with the cloud shield as seen in WV imagery (Figure 16b). The location of the 200 hPa jet streak also contributed to enhanced vertical motion as identified by WV imagery. The colder cloud tops marked the equatorward region of maximum jet streak divergence. Although speed divergence was observed directly over the storm, the divergent region displaced to the northeast suggested that Ma-on may have been located too far west to benefit fully from the jet induced upper-level divergence (Figure 16d).

The two distinct areas of upward motion were identifiable at 500 hPa. The area centered at 145E 39N was a result of jet-streak divergence and the area centered at 138E 34N was due to Ma-on associated dynamics. The omega field also suggested that mid-level subsidence had begun to infiltrate the cyclone center. At this time, AMSU-A data (Figure 20) were available to examine upper-level temperature gradients and will be discussed in section IV.B.2.

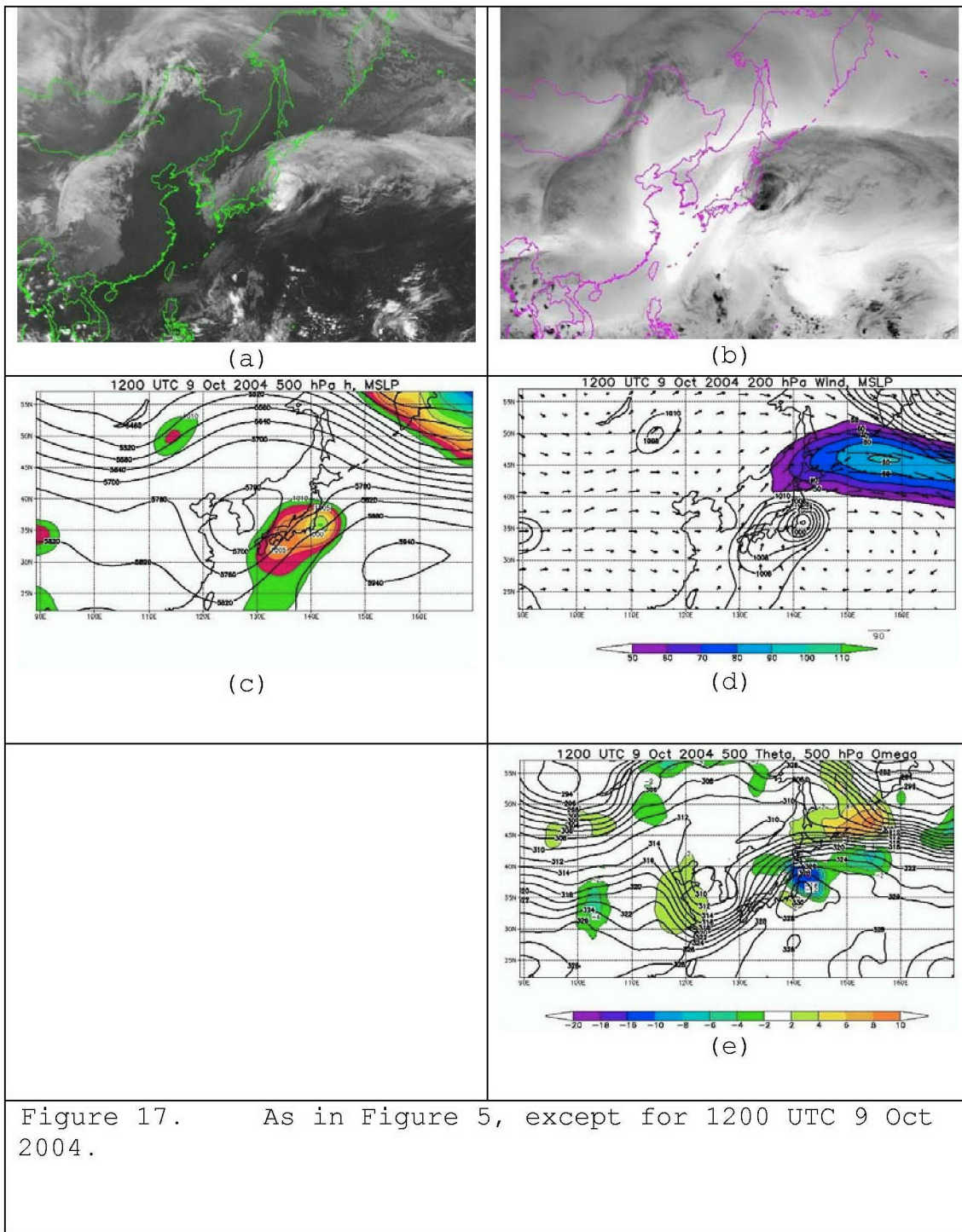


Figure 17. As in Figure 5, except for 1200 UTC 9 Oct 2004.

Ma-on continued to decay over the next 12 h (Figure 17). The TC continued to move northeast but the cloud shield seen on IR imagery remained stationary (Figure 17a). As the storm shifted northward, vertical shear increased (Figure 17c). The IR signature related to deep clouds

continued to decrease as the upper-level storm structure elongated.

The 500 hPa ridge north of the TC shifted east and merged with the subtropical high to the southeast (Figure 17c). As Ma-on moved into the region, the pressure gradient increased between the TC and the ridge to the northeast. The westerly flow, influenced by the ridge to the northeast and the 200 hPa zonal flow, hindered Ma-on's northerly progression.

The mid-level pattern of vertical motion (Figure 17e) intensified between 0000 UTC and 1200 UTC 9 Oct. The storm moved further into the jet streak region and speed divergence above the storm increased. The 500 hPa omega values north of the TC thermal ridge increased in response to the tightening of the pressure gradient in that region. The TC position relative to the jet-induced omega couplet suggested that the jet streak was propagating downstream faster than Ma-on.

By 0000 UTC 10 October (Figure 18), the upper-level circulation was no longer identifiable on IR imagery (Figure 18a). The large anti-cyclonic curvature of the cloud shield after 24 h indicated that a ridge had begun to dominate the region. The increased northwesterly flow between the decaying TC and the quasistationary low to the northeast advected cold air into the region as defined by the open cell cumulus clouds.

The relative storm motion could not be identified via IR imagery, but the MSLP field indicated that the northwesterly progression of the TC had become more westerly (Figure 18c). The MSLP increased to 1008 hPa and

the 500 hPa flow above the TC was now an open wave rather than a closed circulation. Also, the primary 500 hPa trough was farther west over the Sea of Japan as the decaying Ma-on moved into the strong zonal flow directly east of Japan, and ahead of the trough.

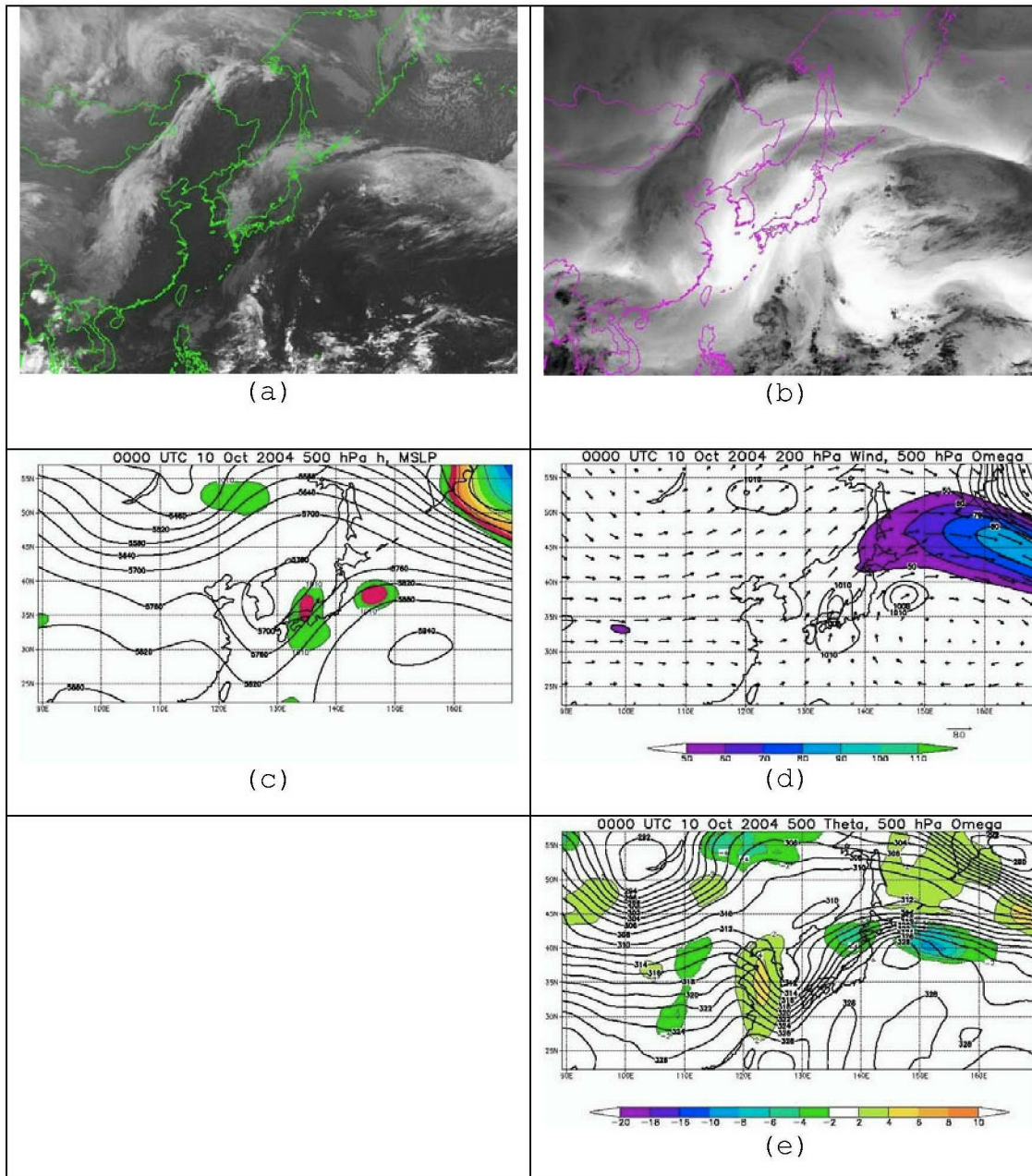


Figure 18. As in Figure 5, except for 0000 UTC 10 Oct 2004.

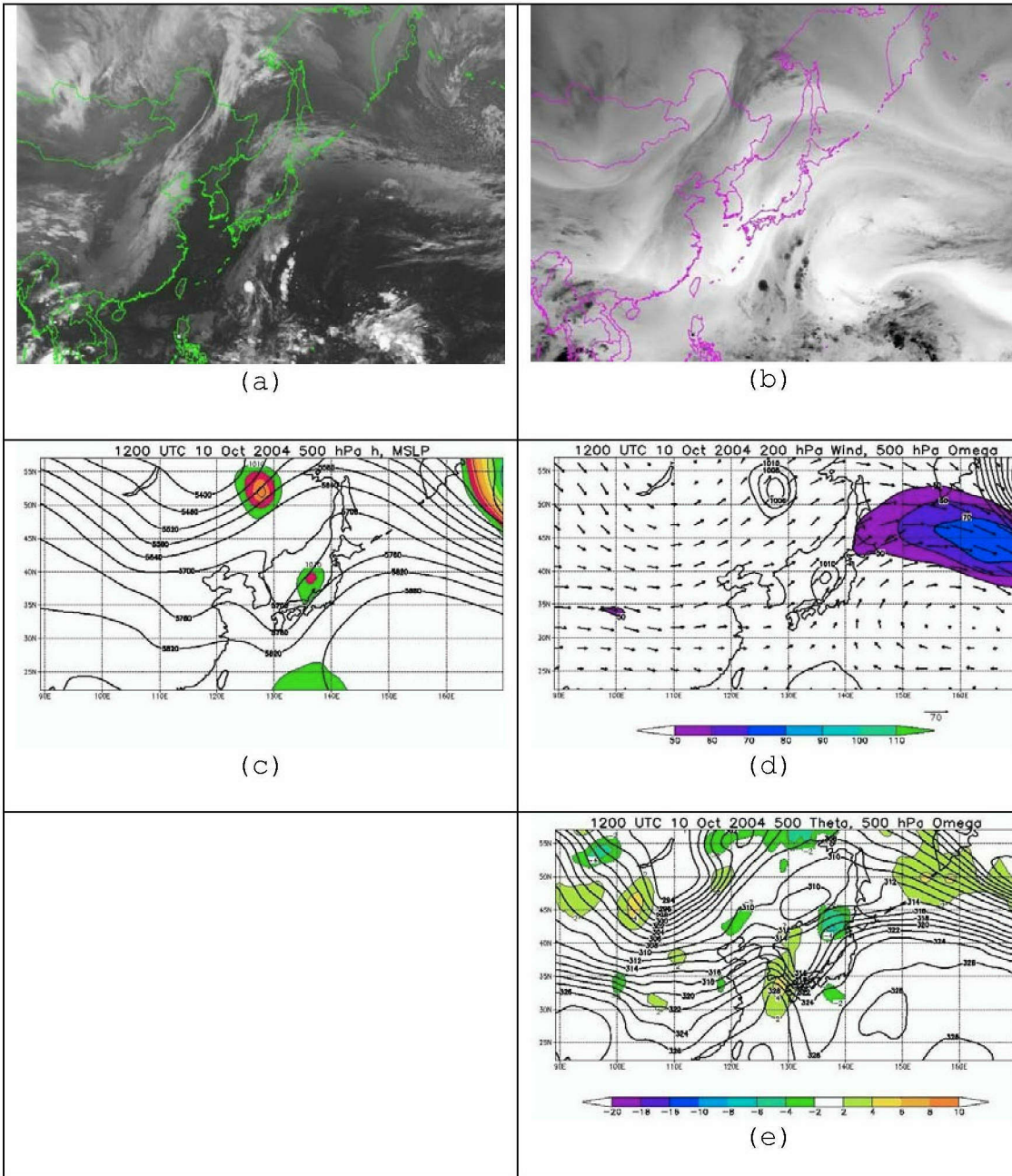


Figure 19. As in Figure 5, except for 1200 UTC 10 Oct 2004.

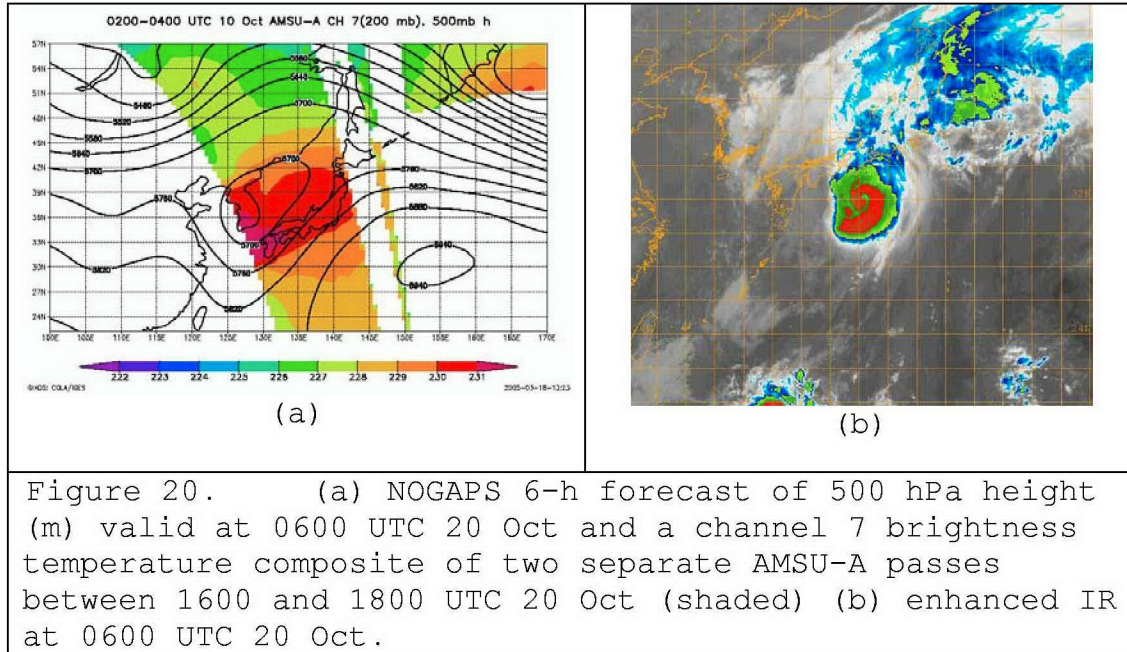
At 1200 UTC 10 Oct 2000 (Figure 19), the midlatitude ridge continued to build over the remnants of Ma-on. The jet streak began to accelerate downstream of the midlatitude ridge. This resulted in a significant decrease in upper-level divergence as it related to Ma-on. The ridge to the north ultimately inhibited Ma-on's progression into the midlatitudes and caused the TC to take more westerly track.

Ma-on failed to enter a re-intensification stage within the 42-h time period. Evidence of the upper-level TC circulation, as identified by WV and IR imagery, did not exist, but convection could be seen between the subtropical high and cyclonic flow behind the TC.

The jet streak continued to shift east ahead of Ma-on (Figure 19d). The TC moved into the area of strong zonal flow between a large midlatitude primary cyclone (60N, 180E) and the subtropical ridge that was east of the decaying TC. The strong zonal flow contributed to strong westerly vertical wind shear. This was responsible for Ma-on's quick decay. Furthermore, the strong pressure and temperature gradients between the primary cyclone and the subtropical high contributed to the rapid translation of the upper-level jet streak. Therefore, Ma-on could not link with the midlatitude dynamics favorable for re-intensification. Ma-on became a representative Northeast ET case based on the definition of Harr and Elsberry (2000).

2. Diagnostics

As with Tokage, AMSU-A was able to identify the upper-level warm core signature (Figure 20) over the decaying TC. However, at this time the upper-level warm area was already elongated ahead of the 500 hPa trough. Because no other



AMSU-A coverage occurred over Ma-on, analysis and diagnostics of Ma-on's transformation depended heavily on AMSR-E precipitation and Petterssen frontogenesis vectors.

The scalar and rotational vectors examined at 0000 UTC 9 Oct (Figure 21) were located in the same region, relative to AMSR-E precipitation, as seen in the beginning stages of Tokage's transformation. The primary rotational frontogenesis forcing was strongly evident in the closed isentropic contours centered at 135E 30N.

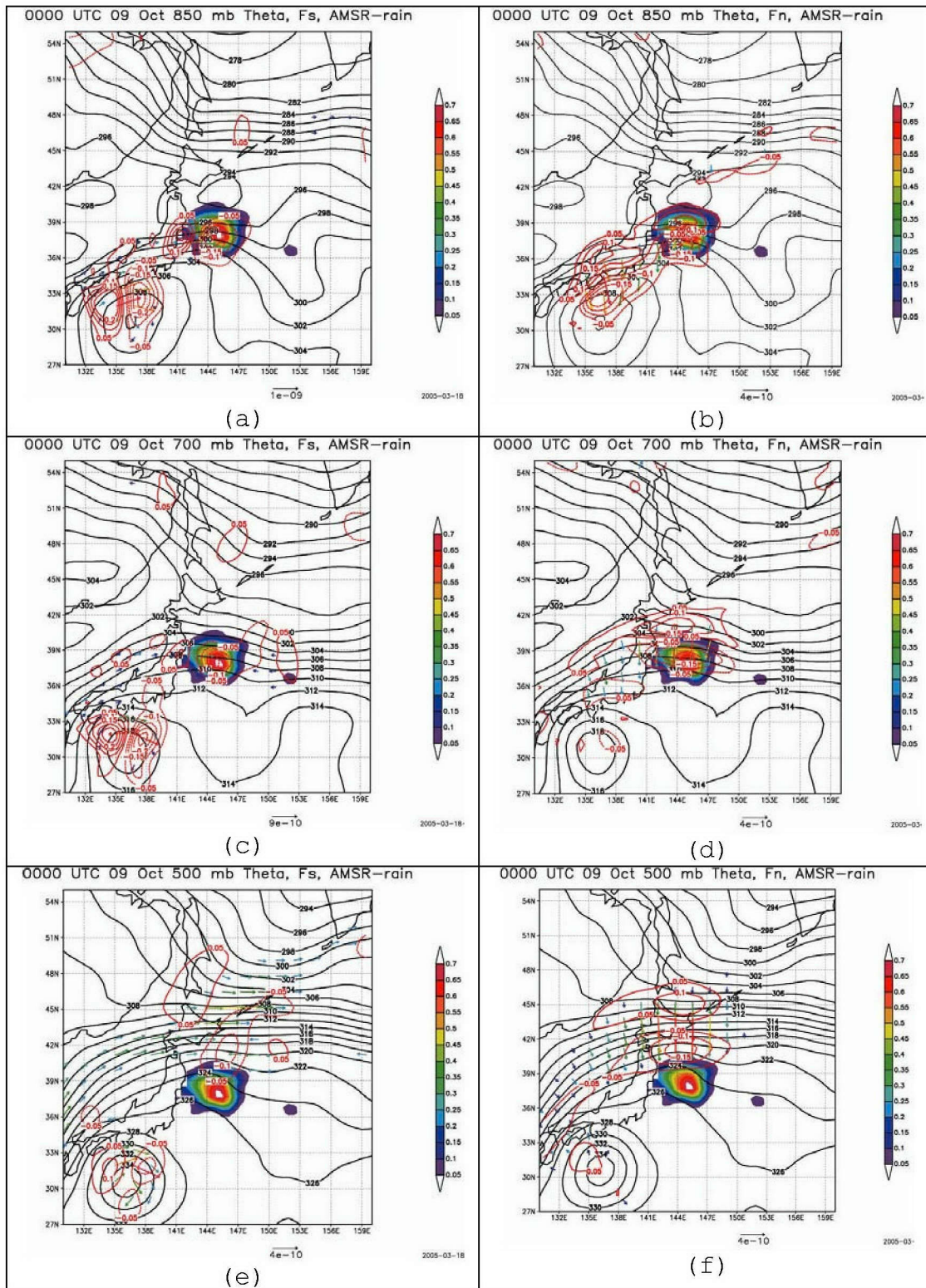
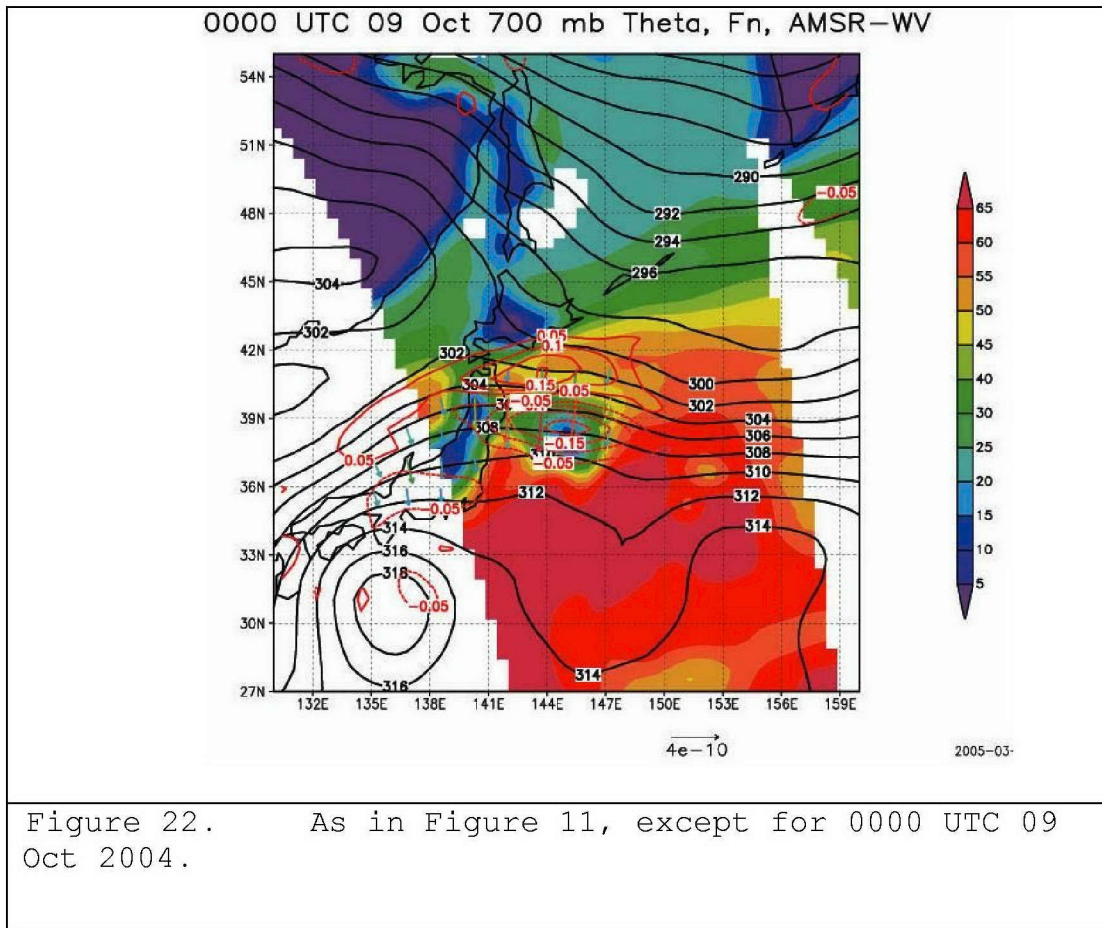


Figure 21. As in Figure 10, except for Typhoon Ma-on 0000 UTC 9 Oct 2004.



The concentration of the 850 hPa scalar vectors (Figure 21b) was equatorward of the max precipitation and extended southwest along the thermal ridge. The scalar contribution to vertical motion extended from the TC center along the thermal ridge to the precipitation region, which indicated that the thermal gradient was increasing poleward of the trough that extended northeast of the TC (Figure 16d). The forcing of vertical motion near the precipitation region at 700 hPa was due primarily to scalar frontogenesis (Figure 21d). Figure 22 indicated that scalar frontogenesis at this level also took place equatorward of the maximum WV gradient. At 500 hPa (Figure 21f), the broad distribution of scalar frontogenesis

defined the influence of synoptic-scale dynamics. The maximum thermal gradient at 500 hPa was positioned between the scalar divergence couplet located poleward of the AMSR-E precipitation. This area, as expected, was co-located with the 200 hPa jet streak (Figure 16d).

At all levels, rotational frontogenesis was highly concentrated around the primary circulation of Ma-on (Figure 21a,c,e). This resulted in a very different distribution of vertical motion than that due to scalar frontogenesis at all levels. There was a vertical motion couplet such that upward motion was being forced east of the decaying TC center and downward motion was being forced west of the center. Therefore, the cyclonic rotation about the decaying center was contributing to an increase in the thermal ridge (WAA) to the east and an increase in the thermal trough to the west (CAA). These vertical motion patterns were similar throughout all levels while the vertical motion due to scalar frontogenesis moved farther northeast of the TC center.

The vertical motion due to scalar frontogenesis coincided with the AMSR-E derived precipitation region and the strong gradient of atmospheric WV (Figure 22). A clear separation was evident in Figure 22 between the remnant TC circulation and the strong midlatitude gradient in potential temperature and WV due to the WAA east of the TC and south of the midlatitude dry air north of the TC. Because of this separation, the decaying Ma-on never fully coupled with the midlatitude dynamics needed for re-intensification.

By 0000 UTC 10 Oct, the dissipation of Ma-on was evident (Figure 18). At this time, both the scalar and

rotational vectors were concentrated north of the thermal ridge (Figure 23a,b). However, the scalar component of frontogenesis continued to be concentrated downstream of the rotational contribution. Also, the precipitation region coincided with the location of scalar frontogenesis at 700 hPa. The rotational component was responsible for the largest contribution to upward motion in the region of the decaying TC.

Tokage and Ma-on began transformation over similar locations with respect to geography and the rear divergent region of a jet streak. However, a major difference existed between the amplitude of the midlatitude ridge north of the TCs. The amplitude of the midlatitude ridge northwest of Tokage was diminished by the midlatitude troughs moving through the region (Figure 5). In contrast, the deepening quasistationary low to the northeast of Ma-on increased the amplitude of the midlatitude ridge.

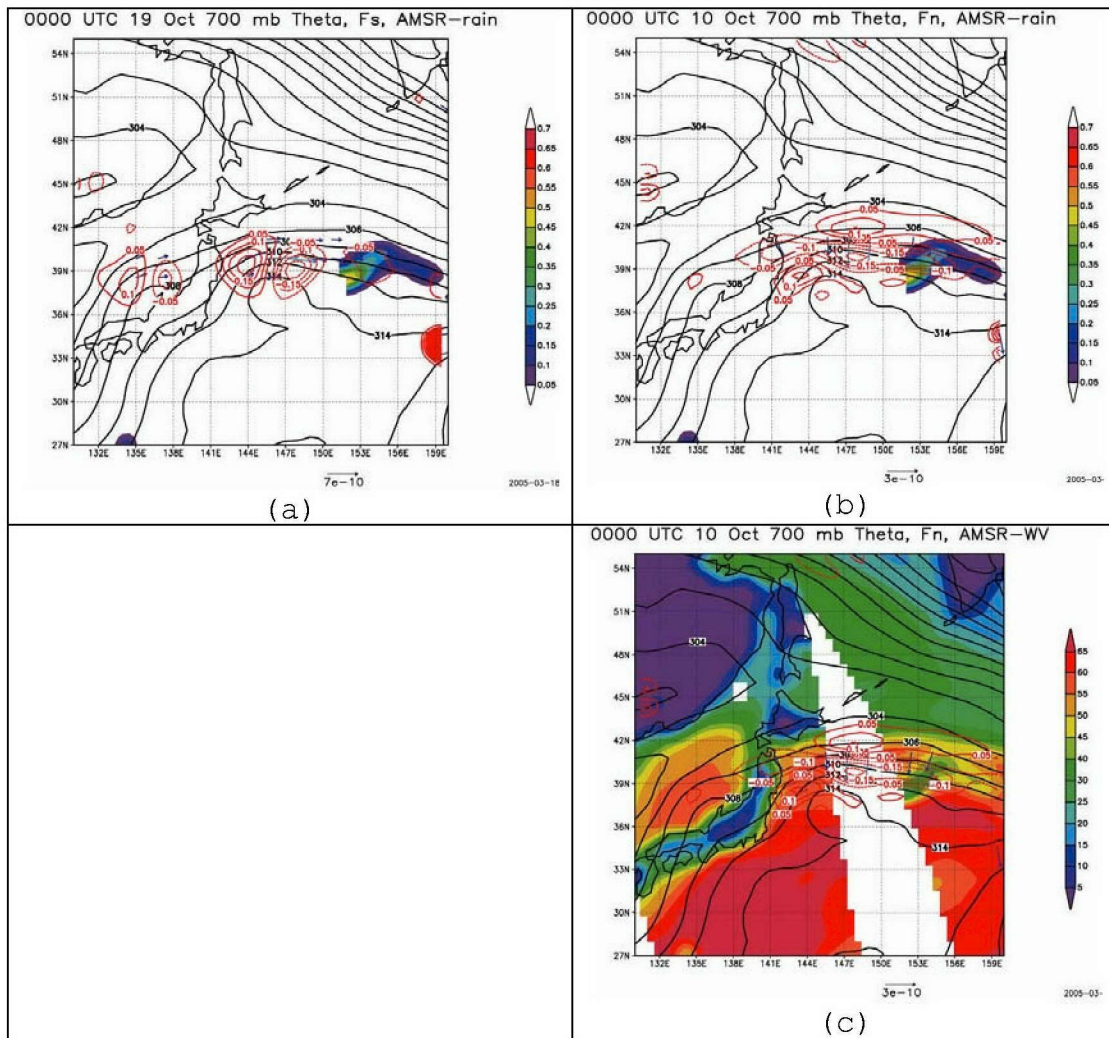


Figure 23. As in Figure 10, except for 0000 UTC 10 Oct 2004

After 12 h into the transformation, IR imagery indicated that shearing by the midlatitude flow had a greater affect on the structure of Ma-on (Figure 17a) than Tokage (Figure 6a). This also was evident in the fact that the 200 hPa jet streak and 500 hPa omega couplet had moved east of Ma-on (Figure 17d,e) but remained over Tokage

(Figure 6d,e). The building ridge, in the case of Ma-on, inhibited upward motion in the region of the TC, which was evident in the relatively large disparity in the 12 h amplitude change as compared to Tokage.

After 24 h into ET, Tokage had begun to develop extratropical characteristics but Ma-on was barely identifiable. Ma-on lost the support of upper-level jet dynamics (Figure 18d) while Tokage remained in the jet streak rear divergent region (Figure 7d). As the midlatitude flow advected Ma-on to the east, the TC began to move in a more westerly direction. However, Tokage continued to move north into the midlatitudes. As Tokage moved to the northeast, WAA continued to build the thermal ridge, but the midlatitude/subtropical ridge inhibited upward motion needed to build the thermal ridge east of Ma-on. Within 36 h of the transformation, Ma-on did not enter the re-intensification stage and subsequently decayed. However, the coupling of the decaying Tokage with the midlatitude dynamics remained conducive for a weak-to-moderate re-intensification.

V. CONCLUSION

This study examined the use of microwave imagery in augmenting diagnostic analysis of the TC ET process of two October TCs in the western Pacific. Imagery from AMSU-A (channel 7), AMSU-B, and AMSR-E were used to investigate storm structure and relative positions of TC dynamics. The results indicated that microwave imagery has the potential to add value to ET diagnostic techniques.

In general, during the transformation stage of ET, the structural evolution of the decaying TC is measured via frontogenesis. Because of the strong circulation characteristics of a decaying TC and the proximity of the strong midlatitude baroclinic zone, it is useful to define frontogenesis in relation to rotation and confluence. Based on diagnostics from analyzed and short-range forecast fields, it has been determined that frontogenesis due to confluence of warm moist air that is advected by the decaying TC toward the midlatitudes dominated the forcing of upward motion and precipitation. Although frontogenesis associated with the circulation of the decaying TC acts to build the thermal ridge east of the TC center, it does not coincide with areas of precipitation that are concentrated northeast of the decaying TC.

The AMSU-A instrument provided a measure of the upper-level thermal structure associated with the TCs in this study. The resolution of channel 7 imagery (estimated at 200 hPa) was sufficient to formulate conclusions concerning the location and horizontal extent of the upper-level warm-core. This is an advantage of utilizing the AMSU-A imagery to examine ET versus a TC as the ET event is dominated by

synoptic scales (hundreds of km) rather than the scales of a TC eye (tens of km). A comparison with IR imagery revealed that AMSU-A imagery can also be used to identify areas of strong WAA advection.

Prior to the start of the transformation stage, AMSU-B imagery was available and identified outflow into the midlatitudes. Not having these data during the transformation stage narrowed the scope of this study. The expectation was that the multiple level moisture capability of AMSU-B imagery would assist in resolving the mid-level moisture redistribution as the TCs became asymmetric.

Derived AMSR-E precipitation and WV imagery were helpful in diagnosing frontogenesis processes. The AMSR-E precipitation proved to be representative of frontogenesis due to confluence caused by warm, moist air in the thermal ridge meeting the cold dry air of the midlatitudes during the transformation stage. The AMSR-E derived WV served as a substitute for AMSU-B imagery in resolving atmospheric WV. The AMSR-E derived WV provided definition of the WV gradient throughout the thermal ridge to the east of each decaying TC. However, WV gradients at different levels of the atmosphere as provided by AMSU-B would have been useful.

The ability to fully exploit the microwave imagery discussed in this study was also hindered by the fact the TCs began their transformation in close proximity to Japan. Choosing a TC that transforms over the open ocean and that is covered sufficiently by microwave passes through the 42 h transformation period will allow for a more complete atmospheric examination of the potential role of microwave imagery in estimating the ET process.

Future study of microwave data applications in estimating the ET process is needed to resolve the relative contribution due to vertical distribution of important atmospheric parameters in the TC and midlatitude environment. Temperature gradients in this study were confined to upper-levels and WV gradients were averaged throughout the atmospheric column. However, microwave imagery is capable of the type of multiple layer analysis that would identify important characteristics of the ET process. This type of analysis may assist in understanding the vertical evolution of the ET process. The increased understanding will lead to improved forecasts of re-intensifying cyclone remnants that often form irregularly moving and irregularly intensifying extratropical cyclones.

THIS PAGE INTENTIONALLY LEFT BLANK

LIST OF REFERENCES

- Advanced Microwave Scanning Radiometer for EOS, cited 2005:
Instrument Description.
[<http://www.ghcc.msfc.nasa.gov/AMSR/>]
- Atallah E.H. and L.F. Bosart 2003: The extratropical transition and precipitation distribution of Hurricane Floyd (1999). *Mon. Wea. Rev.*, 131, 1063-1081.
- Brand, S., and C.P. Guard, 1979: An observational study of extratropical storms that evolved from tropical cyclones in the western North Pacific. *J. Meteor. Soc. Japan*, 57, 479-482.
- Brueske, K.F. 2003: Satellite-based tropical cyclone intensity estimation using the NOAA-KLM Series Advanced Microwave Sounding Unit (AMSU). *Mon. Wea. Rev.*, 131, 687-697.
- DeMaria, M., S.D. Aberson, K.V. Ooyama, and S.J. Lord, 1992: A nested spectral model for hurricane track forecasting. *Mon. Wea. Rev.*, 120, 1628-1643.
- Demuth, J.L. 2004: Evaluation of Advanced Microwave Sounding Unit tropical-cyclone intensity and size estimation algorithms. *J. of Appl. Meteor.*, 43, 282-296.
- DiMego, G.J. and L.F. Bosart, 1982a: The transformation of tropical storm Agnes into an extratropical cyclone. Part I: The observed fields and vertical motion computations. *Mon. Wea. Rev.*, 110, 385-411.
- DiMego, G.J. and L.F. Bosart, 1982b: The transformation of tropical storm Agnes into an extratropical cyclone. Part II: Moisture, vorticity and kinetic energy budgets. *Mon. Wea. Rev.*, 110, 412-433.
- Dvorak, V.F., 1975: Tropical cyclone intensity analysis and forecasting from satellite imagery. *Mon. Wea. Rev.*, 103, 420-430.
- Evans, J.L., and R.E. Hart, 2003: Objective indicators of the live cycle evolution of extratropical transition for Atlantic tropical cyclones. *Mon. Wea. Rev.*, 131, 909-925. and
- Foley, G.R., and B.N. Hanstrum, 1994: The capture of tropical cyclones by cold fronts off the west coast of Australia. *Wea. Forecasting*, 9, 577-592.
- Goldberg, M.D., 2001: The Limb adjustment of AMSU-A observations: Methodology and validation. *J. Appl. Meteor.*, 40, 70-83.

- Goodrum, G., K.B. Kidwell, and W. Winston, (eds.) 2004: NOAA KLM user's guide. NOAA, NOAA-NESDIS/NCDC, Suitland, Maryland, USA.
- Harr, P. A., and R.L. Elsberry, 2000: Extratropical transition of tropical cyclones over the western North Pacific. Part I: Evolution of structural characteristics during the transition process. *Mon Wea. Rev.*, 128, 2613-2633.
- , and ----, and T. Hogan 2000: Extratropical transition of tropical cyclones over the western North Pacific. Part II: The impact of midlatitude circulation characteristics. *Mon Wea. Rev.*, 128, 2634-2653.
- Heming, J.T., and A.M. Radford, 1998: the performance of the United Kingdom Meteorological Office global model in predicting the tracks of Atlantic tropical cyclones in 1995. *Mon. Wea. Rev.*, 126, 1323-1331.
- Jones, S.C., P. Harr, J. Abraham, L.F. Bosart, P.J. Bowyer, J. L. Evans, D.E. Hanley, B.N. Hanstrum, R.E. Hart, F. LaLaurete, M.R. Sinclair, R.K. Smith, and C. Thorncroft, 2003: The extratropical transition of tropical cyclones: forecast challenges, current understanding, and future Directions. *Wea. Forecasting*, 18, 1052-1092
- Keyser, D. 1988: A generalization of Petterssen's frontogenesis function and its relation to the forcing of vertical motion. *Mon. Wea. Rev.*, 116, 762-780
- Klein, P., M., P.A. Harr, and R.L. Elsberry, 2000: Extratropical transition of western Pacific tropical cyclones: An overview and conceptual model of the transformation stage. *Wea. Forecasting*, 15, 373-396
- Kurihara, Y., M.A. Bender, and R.J. Ross, 1993: An initialization scheme of hurricane models by vortex specification. *Mon. Wea. Rev.*, 121, 2030-2045.
- Liu, Guosheng 2004: Description of precipitation retrieval algorithm for ADEDS II AMSR. ERRC Bulletin/Technical Report available at <http://www.orbit.nesdis.noaa.gov/corp/scsb/wchen/AMSR-E/>.
- Matano, H., and M. Sekioka, 1971a: On the synoptic structure of Typhoon Cora, 1969, as the compound system of tropical and extratropical cyclones. *J. Meteor. Soc. Japan*, 49, 282-295.
- Mo, T., 1999: AMSU-A antenna pattern corrections. *IEE Trans. Geosci. Remote Sens.*, 37, 103-112

- Muramatsu, T., 1985: A study on the changes of the three-dimensional structure and movement speed of the typhoon through its life time. Meteorological Research Institute Tech. Rep. 14, Japan Meteorological Agency, 117 pp.
- Palmen, E., 1958: Vertical circulation and release of kinetic energy during the development of hurricane Hazel into an extratropical storm. *Tellus*, 10, 1-23.
- Pierce, C., 1939: The meteorological history of the New England hurricane of Sept. 21, 1938. *Mon. Wea. Rev.*, 67, 237-288.
- Pu, Z.X. and S.A. Braun, 2001: Evaluation of bogus vortex techniques with four-dimensional variational data assimilation. *Mon. Wea. Rev.*, 129, 2023-2039.
- Sinclair, M.R., 1993a: A diagnostic study of the extratropical precipitation resulting from Cyclone Bola. *Mon. Wea. Rev.*, 121, 2690-2707.

THIS PAGE INTENTIONALLY LEFT BLANK

INITIAL DISTRIBUTION LIST

1. Defense Technical Information Center
Ft. Belvoir, Virginia
2. Dudley Knox Library
Naval Postgraduate School
Monterey, California
3. Superintendent
Naval Research Laboratory
Monterey, California
4. Professor Patrick Harr
Naval Postgraduate School
Monterey, California
5. Professor Phil Durkee
Naval Postgraduate School
Monterey, California
6. Director, Joint Typhoon Warning Center
Naval Pacific Meteorology and Oceanography Center
Pearl Harbor, Hawaii
7. Captain Cedrick Stubblefield
Air Force Weather Agency
Offutt AFB, Nebraska